# Phase diagram, susceptibility, and magnetostriction of MnP: Evidence for a Lifshitz point

Y. Shapira
*Francis Bitter National Magnet Laboratory, Massachusetts Institute of Technology, Cambridge, Massachusetts 02139*

C. C. Becerra and N. F. Oliveira, Jr.
*Instituto de Fisica, Universidade de São Paulo, C.P. 20516, São Paulo, Brazil*

T. S. Chang
*Center for Space Research, Massachusetts Institute of Technology, Cambridge, Massachusetts 02139*

(Received 23 February 1981)

The phase diagram of MnP was determined from magnetostriction and differential susceptibility measurements. Data were taken from 4.2 K up to the Curie temperature $T_C = 290.9$ K. The applied magnetic field $\vec{H}_0$ was parallel to the $b$ axis. The focus of the measurements was on the upper triple point ($T = 121 \pm 1$ K, $H_0 \cong 16.5$ kOe) where the paramagnetic (para), ferromagnetic (ferro), and fan phases meet. The transitions on the para-ferro boundary $H_{0\lambda}(T)$ and on the para-fan boundary $H^*_{0\lambda}(T)$ were of second order. The ferro-fan transitions on the boundary $H_{01}(T)$ were of first order. At the upper triple point, all three phase boundaries were tangent to each other, and the $\lambda$ line [composed of the boundaries $H_{0\lambda}(T)$ and $H^*_{0\lambda}(T)$] had an inflection point. These qualitative features agree with those expected at a Lifshitz point (LP). A quantitative analysis of the difference $H^*_{0\lambda} - H_{01}$ as a function of $T$ gave a crossover exponent $\phi = 0.63 \pm 0.04$. This value agrees with the calculated value for the LP. The correspondence between the scaling axes near the upper triple point and those in the theory of the LP is discussed. The phase diagram near the upper triple point was also measured as a function of the angle $\theta$ between $\vec{H}_0$ and the $b$ axis. The field $\vec{H}_0$ was in the $bc$ plane, and its $c$ component $H_{0c}$ played the role of the ordering field for the ferro phase. The results were interpreted in terms of predictions for a LP, supplemented by considerations of demagnetization effects. In addition to the usual parallel differential susceptibility, $\partial M/\partial H_0$, the transverse differential susceptibility was also measured near the upper triple point. Here, the applied dc field $\vec{H}_0$ was parallel to $b$, the applied modulation field $\vec{h}_0$ was parallel to $c$, and the measured quantity was $\partial M_c/\partial h_0$. The transverse susceptibility showed the features expected near a LP. Additional evidence, from two recent neutron studies, that the upper triple point is a LP is summarized. The global phase diagram of MnP, the para-ferro boundary near $T_C$, and the screw-ferro transition at $T_\alpha = 46$ K, are also discussed.

## I. INTRODUCTION

Recent theoretical activity concerning the Lifshitz point[1] has stimulated experimental attempts to observe this multicritical point in a real physical system. In the present work we describe such an attempt, and show that the data which we obtained in MnP are in agreement with those expected for a Lifshitz point.

Magnetic materials exhibit a variety of magnetic orders. Among them are the ferromagnetic order in which the magnetization is uniform in space, and the helicoidal order in which the magnetization varies in space with a periodicity which is characterized by a wave vector $\vec{q}$. Simple examples in which the helicoidal order is preferred over a ferromagnetic (or antiferromagnetic) order can be constructed by considering appropriate combinations of competing exchange interactions.[2] The wave vector $\vec{q}$ of the helicoidal phase may depend on parameters such as pressure $P$, temperature $T$, magnetic field $\vec{H}$, or material composition. For example, the pressure may affect the relative strengths of the competing exchange interactions, resulting in a change of $\vec{q}$. The transition temperature $T^*_\lambda$ from the disordered paramagnetic (para) phase to the ordered helicoidal phase will then depend on $P$. If the ordered phase is ferromagnetic (ferro), then the para-ferro ordering temperature $T_\lambda$ also will depend on $P$. The transi-

 

tions at both $T_\lambda^*$ and $T_\lambda$ are assumed to be of second order.

Consider a magnetic system which has a helicoidal phase. An interesting situation arises when the wave vector $\vec{q}$ can be tuned continuously to zero by changing the pressure or some other thermodynamic parameter. In that case, the system possesses both helicoidal ($\vec{q} \neq 0$) and ferro ($\vec{q} = 0$) ordered phases. The phase diagram in the $TP$ plane then consists of (at least) three phases: para, ferro, and helicoidal. The three phases meet at a triple point. This triple point divides the $\lambda$ line into two segments: the para-helicoidal segment $T_\lambda^*(P)$, and the para-ferro segment $T_\lambda(P)$. Such a triple point is called a ferromagnetic Lifshitz point. In addition to the two segments of the $\lambda$ line, there is also a phase boundary $T_1(P)$ between the ferro and helicoidal phases. The phase diagram is sketched in Fig. 1.

The Lifshitz point (LP) was introduced theoretically by Hornreich, Luban, and Shtrikman.[3] Since then, considerable theoretical efforts have been devoted to this multicritical point.[1] As pointed out in Ref. 1, there are other types of Lifshitz points besides a ferromagnetic LP. In general, the ferro phase ($\vec{q} = 0$) may be replaced by a phase with $\vec{q} = \vec{q}_0 = \text{const}$. Then the wave vector $\vec{q}$ in the helicoidal phase approaches $\vec{q}_0$ continuously as the LP is approached. Lifshitz points may also exist in nonmagnetic systems, such as liquid crystals and crystals undergoing structural phase changes. More general types of Lifshitz points than those introduced in Ref. 3 were also discussed.[4] For present purposes it will be sufficient to consider ferromagnetic Lifshitz points only.

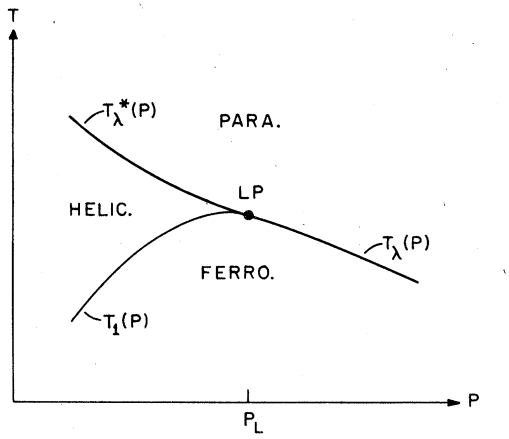


FIG. 1. Schematic for the phase diagram near a Lifshitz point (LP). $T$ and $P$ are temperature and pressure, respectively. The heavy line is the $\lambda$ line between the disordered para phase and the two ordered phases (ferro and helicoidal). The $\lambda$ line has two segments: $T_\lambda(P)$ and $T_\lambda^*(P)$. The light line is the phase boundary $T_1(P)$ between the two ordered phases.

A relatively simple model which exhibits a LP is that of a simple cubic material with ferromagnetic nearest-neighbor interaction, and a competing antiferromagnetic interaction between next-nearest neighbors along a single cubic axis.[5,6] If $J_1$ and $J_2$ are the nearest-neighbor and next-nearest-neighbor exchange constants then mean-field theory gives a LP at $J_2/J_1 = -0.25$, whereas high-temperatures-series calculations for Ising spins give a LP at $J_2/J_1 = -0.27$.[5] It is noteworthy that the same model with Ising spins [so-called anisotropic next-nearest-neighbor Ising (ANNNI) model] has interesting properties other than the LP.[7]

A more general treatment of the LP starts from a Landau-type expansion for the free-energy density $F$, including contributions from the spatial derivatives of the order parameter.[1] For an isotropic system with a scalar order parameter $M$,

$$F = a_2 M^2 + a_4 M^4 + a_6 M^6 + \cdots + \alpha(\nabla M)^2 + \beta(\nabla^2 M)^2 + \cdots \quad . \tag{1}$$

It is assumed that the coefficient $\beta$ is positive. The coefficient $\alpha$ is assumed to depend on $P$, and to change its sign at $P = P_L$. When $\alpha(P)$ is positive, a ferromagnetic order is established. When $\alpha(P)$ is negative, an helicoidal order is established. The LP occurs at the pressure $P_L$ where $\alpha$ vanishes. For this isotropic example the number of components of $\vec{q}$ in the helicoidal phase is equal to the spatial dimensionality $d$. For anistropic crystals, the number $m$ of components (for the vector $\vec{q}$) may be smaller than $d$. Thus, in general, $m \leq d$. In addition, $\vec{M}$ may be a vector with $n$ components rather than a scalar. Thus, a LP is characterized by $d$, $n$, and $m$.

The allowed types of ferromagnetic Lifshitz points for different crystallographic structures were discussed by Hornreich.[8] For a (three-dimensional) orthorhombic crystal, such as the one investigated in the present work, a ferromagnetic LP should be characterized by $d = 3$, $n = m = 1$.

In contrast to the numerous theoretical results for the LP, previous experimental evidence for the existence of a LP was scant and tenuous. The difficulty of observing a LP stems from the insensitivity of the parameter $\alpha$, in most materials, to changes in thermodynamic variables such as $P$. Thus, $\alpha$ must be initially quite close to zero if it is to change its sign as a function of an experimental variable. In addition, some promising candidates for observing a LP undergo a first-order transition from the disordered phase to the ordered phase (or phases), instead of the required second-order transition. Among the previous experimental works on the LP are the measurements on the uniaxially stressed $RbCaF_3$, which suggested a tricritical Lifshitz behavior.[9] Very recently, Sinha *et al.*[10] carried out a neutron study on UAs, and concluded that the transition was near a LP. However, the observed transition was of first order. Moreover,

the ordered phase (which was commensurate) had a fixed $\vec{q}_0$ which differed appreciably from the wave vector $\vec{q}$ of the competing helicoidal phase. At a true LP, the transition is of second order, and $\vec{q} \rightarrow \vec{q}_0$.

The present work on MnP was motivated by previous data on this material, which are summarized in Sec. II. These data showed that MnP possesses ferro and helicoidal phases which meet the para phase at a triple point. Although the available data for the phase boundaries near this triple point appeared to be inconsistent with a LP, we suspected that a closer study might lead to the opposite conclusion. Accordingly we have undertaken detailed measurements of the phase boundaries near this triple point. We also carried out susceptibility measurements in an experimental configuration for which characteristic features of the LP should be observed. Both types of measurements strongly suggested that the triple point was a LP. A preliminary report was then published.[11] The present paper contains a detailed exposition of these results, as well as data for the entire phase diagram (i.e., not only near the triple point). The dependence of the phase diagram on the ordering field for the ferro phase is also discussed.

In addition to the phase boundaries and susceptibility data which are presented here, there is now strong evidence for a LP in MnP from a neutron study of $\vec{q}$ in the relevant helicoidal phase,[12] and also from another neutron study of the dispersion curves for spin waves.[13]

This paper is arranged as follows. Some properties of MnP which are relevant to the present study are summarized in Sec. II. The experimental techniques are reviewed in Sec. III. The phase diagram, with emphasis on the para-ferro-helicoidal triple point, is presented in Sec. IV. The phase diagram near this upper triple point is analyzed in Sec. V. Data for the dependence of the phase diagram on the orientation of the magnetic field are presented in Sec. VI. In Sec. VII susceptibility data that show expected features of a LP are presented. In Sec. VIII we conclude by reviewing the evidence for a LP in MnP.

## II. SOME PROPERTIES OF MnP

Manganese phosphide has an orthorhombic structure. Two choices of the orthorhombic axes have been used in the literature. Here we shall use the choice $a > b > c$ ($a = 5.92$ Å, $b = 5.26$ Å, and $c = 3.17$ Å), which is the more common in the recent literature. MnP is metallic and exhibits several magnetic phases which have been the subject of many investigations for more than a decade. These investigations included measurements of the magnetization,[14–16] differential magnetization,[17] torque,[18] thermal expansion,[19–21] magnetostriction,[19,22] ultrasonic attenuation,[23,24] resistivity,[25,26] magnetoresistance,[15,27,28] Bragg scattering of neutrons,[12,29–33] spin-wave dispersion curves,[13,34] dependence of transition temperatures on hydrostatic and uniaxial pressures,[19,35,36] and the de Haas–van Alphen effect.[37]

At zero magnetic field MnP undergoes a para-ferro transition at the Curie point $T_C = 291$ K.[14] Below $T_C$, the ferromagnetic moment is parallel to the $c$ axis, and the $b$ and $a$ axes are the intermediate and hard axes, respectively. The transition at $T_C$ is of second order. The critical behavior near $T_C$ was investigated by several workers.[16,21,24]

If $H$ is maintained at zero, a second magnetic phase is observed at temperatures below $T_\alpha \cong 47$ K. Neutron-diffraction experiments[29,30,33] indicate that this low-temperature phase is a spiral with a propagation vector $\vec{q}$ which is parallel to the $a$ axis, and whose magnitude corresponds to a period of nine lattice spacings approximately. This spiral phase is known as the screw phase. The local magnetic moment in this phase rotates in the $bc$ plane as one advances along the $a$ direction. Pictorial representations of the magnetic order in the screw phase are given in Refs. 29 and 30. The zero-field transition at $T_\alpha$ (from the high-temperature ferro phase to the low-temperature screw phase) is of first order. The value of $T_\alpha$ is slightly dependent on sample purity.[26]

When a magnetic field $\vec{H}$ is applied parallel to the $b$ direction, a second helicoidal phase is observed in a certain range of temperatures and fields. In this phase also, $\vec{q}$ is parallel to $a$.[31] However, the local magnetic moment does not undergo a full rotation in the $bc$ plane as one advances along the $a$ direction. Instead, the moment wobbles about the $b$ direction, remaining always in the $bc$ plane.[15] Because the magnetic order resembles a fan, the phase is known as the fan phase.

The salient features of the phase diagram in the $TH$ plane, for $\vec{H} \parallel b$, were determined in earlier investigations.[15,22] In Fig. 2 we show our own results for the global phase diagram. The gross features of this figure are similar to those observed earlier. Four phases are present: para, ferro, fan, and screw. The first three phases meet at an upper triple point (para-ferro-fan triple point), while the last three meet at a lower triple point (ferro-fan-screw triple point). A crucial difference between our detailed measurements of the phase diagram and the earlier data is that the phase boundaries near the upper triple point do not meet at finite angles, but instead are tangent to each other. The main focus of our work was on this para-ferro-fan triple point.

Early investigations (e.g., Ref. 15) showed that the para-ferro and para-fan transitions are of second order. It is believed that the para-to-ferro transition is associated with the development of a uniform magnetization component parallel to the $c$ axis. As $H$ decreases, this component, $M_c$, increases while the $b$ magnetization component, $M_b$, decreases. As $H \rightarrow 0$,

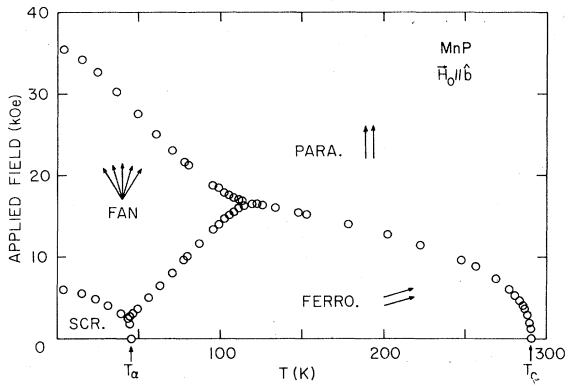


FIG. 2. Phase diagram of MnP, for applied magnetic field $\vec{H}_0$ parallel to $b$. These data were obtained from magnetostriction and thermal expansion measurements on sample 3. The screw phase is designated as SCR. Some data points were deleted, to avoid overcrowding.

the magnetic moment in the ferro phase becomes parallel to the $c$ axis. Because the $\pm c$ directions are equivalent, one expects two types of domains in the ferro phase, with opposite signs for $M_c$, but with the same $M_b$. The para-to-fan transition is associated with the development of an oscillatory magnetization component along the $c$ axis. In the fan phase, the magnitude of this oscillatory $c$ component increases with decreasing $H$. Near both the para-ferro and para-fan transitions there is a continuous variation of $M_b$. All the transitions between the magnetically ordered phases (i.e., ferro-fan, ferro-screw, and screw-fan) are of first order.

Early neutron diffraction data[31] showed that at 77 K the magnitude of $q$ in the fan phase corresponded to a period of order of ten lattice spacings, and that $q$ was $H$ dependent. This meant that $q$ could be tuned by changing thermodynamic parameters.

Very recently the spin-wave dispersion curves, $\omega$ vs $k$, were determined at $H=0$ as a function of $T$.[13] For spin waves with wave vector $\vec{k}$ parallel to $a$, the dispersion curves are relatively flat for small $k$, and they show a marked dependence on $T$. The dispersion curves for $\vec{k} \| a$ were fitted to a model with two exchange constants, $J_1$ and $J_2$. This model is similar to that mentioned in Sec. I. The data led to values of $J_2/J_1$ which were slightly $T$ dependent, but were near $-0.25$. Such values for $J_2/J_1$ are close to those expected at a LP (see Sec. I). Moreover, because $J_2/J_1$ changes with $T$, one might expect that at some particular temperature this ratio will match that at a LP.

## III. EXPERIMENTAL TECHNIQUES

### A. Samples

The three samples which were used in the present experiments were cut from one single crystal which was grown more than a decade ago in the Lincoln Laboratory, MIT. All samples were rectangular parallelepipeds, with faces parallel to the $a$, $b$, and $c$ crystallographic faces. The linear dimensions, $l_i$, along the $i$th crystallographic direction were as follows. For sample 1: $l_a=4.0$ mm, $l_b=3.0$ mm, $l_c=0.5$ mm. For sample 2: $l_a=0.97$ mm, $l_b=2.67$ mm, $l_c=0.84$ mm. For sample 3: $l_a=0.9$ mm, $l_b=2.6$ mm, $l_c=2.6$ mm. The shapes of the samples are significant because the demagnetizing field (which was important in some cases) depended, in part, on the sample's dimensions. It is noteworthy that the recent neutron Bragg scattering experiments[12] were carried out on sample 3.

Measurements of the resistivity $\rho$ of sample 2 (performed at $H=0$, with the electric current along $b$) gave $\rho(273\text{ K})/\rho(4.2\text{ K})=67$.

### B. Susceptibility measurements

The isothermal differential susceptibility $\partial M_i/\partial h_0$ was measured by applying a small oscillatory magnetic field $\vec{h}_0$ (superimposed on the applied dc field $\vec{H}_0$) and measuring the periodic change in a component $M_i$ of the net magnetization $\vec{M}$ of the sample. Two types of susceptibility measurements were performed: parallel and perpendicular. By parallel susceptibility we mean a situation in which $\vec{h}_0$ is parallel to $\vec{H}_0$, and $M_i=M_H$ is the component of $\vec{M}$ along $\vec{H}_0$. In this case, $\partial M_i/\partial h_0=\partial M_H/\partial H_0$. All the data for $\partial M_H/\partial H_0$ were taken with $\vec{H}_0$ parallel to a symmetry axis, so that $M_H$ was equal to $M$. Thus, the parallel differential susceptibility was $\partial M/\partial H_0$.

By perpendicular susceptibility we mean a situation in which $\vec{h}_0$ is perpendicular to $\vec{H}_0$, and $M_i=M_h$ is the component of $\vec{M}$ along $\vec{h}_0$. This terminology differs from the standard usage of the term "perpendicular susceptibility." Ordinarily the differential susceptibility which is measured is $\partial M_H/\partial H_0$, and the terms "parallel" and "perpendicular" refer to the direction of $\vec{H}_0$ relative to the easy magnetization direction. Measurements with a modulation field $\vec{h}_0$ perpendicular to $\vec{H}_0$ are not common, and there is no standard terminology to describe them. Our terminology is useful for present purposes.

The measurements of the parallel and perpendicular differential susceptibilities were performed in two different laboratories (at USP and at MIT, respectively). The measurement techniques were somewhat different.

#### *1. Parallel differential susceptibility*

The parallel differential susceptibility $\partial M/\partial H_0$ was measured with an ac mutual inductance bridge, similar to that described by Maxwell.[38] The arrangement included a primary modulation coil, and a set of two pickup coils wound in opposition and serving as a

secondary. During the measurements the sample was placed inside one of the secondary coils. The frequency of the modulation field $h_0$ was 1550 Hz, and its amplitude was 3 Oe. Checks made with frequencies as low as 50 Hz showed that the phase boundaries which were determined from the susceptibility data were independent of the measuring frequency. The measurements were carried out in a NbTi superconducting magnet with a 51-mm-diam bore. The field homogeneity near the center of this magnet was 0.01% over a 25-mm-diam sphere. The field calibration was accurate to 1%. The field was read with a precision of 10 Oe.

Data for $\partial M/\partial H_0$ were taken between 80 and 150 K. The cryogenic arrangement was as follows. An insert Dewar (anti-Dewar) consisting of a double-wall, vacuum-insulated, stainless-steel tube was inserted into the bore of the magnet. The inside of this insert Dewar was connected to the liquid-helium bath of the magnet by a small tube equipped with a needle valve which was controlled from the top of the cryostat.[39] An adjustable stream of cold liquid vapor was produced inside the insert Dewar by controlling the needle valve and by pumping with different speeds on the insert Dewar.

A second Dewar consisting of a long, vacuum-insulated, double-wall, glass tube was placed inside the insert Dewar. This glass Dewar was supported from the top by a stainless-steel tube, as described by Oliveira and Quadros.[40] A manganin heater was placed outside this glass Dewar. A 370-$\Omega$, 0.125-W, Allen-Bradley carbon resistance thermometer was also placed outside the glass Dewar, and served as the temperature sensor for a feedback loop which controlled the heater. The magnetoresistance of the carbon thermometer was negligible. By controlling the stream of helium vapor inside the insert Dewar, and the heater, the temperature outside the glass Dewar was held constant to within 0.1 K. The temperature inside the glass Dewar was then constant to within 0.01 K for periods as long as 1 h.

The primary coil of the mutual inductance bridge was attached to the outer wall of the glass Dewar, but the set of secondary coils was inside this Dewar. The sample was housed in a cylindrical capsule made of epoxy resin. The capsule fitted snugly into one of the secondary pickup coils. The temperature of the sample was measured with a platinum resistance thermometer. Thermal contact between this thermometer and the sample was through strips of "coil foil"[41] which were attached to both the thermometer and the sample by cotton threads and Apiezon-N grease. Additional thermal contact was through helium gas which was present in the glass Dewar. The magnetoresistance of the platinum thermometer was calibrated and was corrected for. At the temperatures and fields which were used, this magnetoresistance was equivalent to 0.03 K or less.

### 2. *Transverse differential susceptibility*

The transverse differential susceptibility was measured using a set of primary modulation coils, and a set of two pickup coils wound in opposition and serving as a secondary. The set of primary modulation coils consisted of two separate coils which were attached to the outer surface of the tail of a glass Dewar. These two coils were on opposite sides of the tail. They were connected so that their magnetic fields (inside the tail and on a line joining the centers of the coils) were in the same direction. To optimize the homogeneity of $\vec{h}_0$, the design of Ref. 42 was followed. The dc field $\vec{H}_0$ was in the vertical direction (along the axis of the Dewar), and $\vec{h}_0$ was in a horizontal direction.

*Each* of the two secondary coils consisted of a pair of coaxial coils which were wound in the same direction, and which were separated by a small gap (i.e., resembling a pair of Helmholtz coils). The common axis of the pair was parallel to $\vec{h}_0$. The sample could be moved in and out of the gap separating the pair by changing its vertical position. The entire assembly of secondary coils consisted, therefore, of two Helmholtz-like pairs which were wound in opposition to each other. These two pairs were placed one above the other.

The susceptibility measurements were performed by monitoring the imbalance voltage between the two secondary coils, with the sample in one of the coils. The imbalance signal was measured with a lock-in amplifier whose output in the absence of a sample and at $H=0$ was adjusted to zero. The phase of the lock-in amplifier was adjusted so that only the real part of the susceptibility was measured. (This was the phase where the voltage from either Helmholtz-like pair was maximum in the absence of the sample. A check of the quadrature signal from the sample showed that it was only 3–4% of the in-phase signal from the sample, for $88 < T < 140$ K. The quadrature signal did not vary appreciably with $H$. The smallness of the quadrature signal indicated that losses caused by the finite conductivity of the sample had a negligible effect on the results for the $T$ and $H$ dependences of the susceptbility.) The frequency and amplitude of $h_0$ were 188 Hz and 4 Oe, respectively.

A major difficulty was the vibration of the primary modulation coils, which was caused by ac torques. The torques were related to the fact that $\vec{h}_0$ was perpendicular to $\vec{H}_0$. To reduce the vibration we used the following precautions: (1) The primary coils were impregnated with epoxy while the coils were wound. (2) The primary coils were epoxied to the tail of the glass Dewar. (3) The motion of this tail was reduced by attaching its lower end to a heavy cylinder which rested on the ground. With these precautions, the background caused by the vibration was a small frac-

tion of the signal from the sample. To eliminate the small remaining background, the following procedure was used. The imbalance signal from the two secondary coils was first measured as a function of $H_0$, with the sample in one of these coils. The measurement was repeated with the sample in the other secondary coil. The susceptibility of the sample, as a function of $H_0$, was then obtained by subtracting the two traces. The data acquisition was automated, and the data processing was performed with the aid of a small computer.

The susceptibility measurements were performed in a Bitter-type magnet with a bore of 254 mm. The unusually large bore allowed the glass Dewar to be tipped by up to several degrees. This option was used to align $\vec{H}_0$ parallel to the $b$ axis of the sample. The measurements were carried out at 88 K, and at several fixed temperatures between 103 and 146 K. The data at 88 K were taken with liquid argon inside the glass Dewar. The higher temperatures were produced in a bath of Freon 14 whose vapor pressure was regulated. To achieve temperature stability in the Freon-14 bath (particularly at the lowest temperatures), a heater was placed at the bottom of the Dewar. The heat input was sufficient to produce bubbles in the bath. In addition, the hydrostatic head was kept small. Temperatures were measured with a platinum resistance thermometer, which was inside the liquid bath and close to the secondary coils.

### C. Magnetostriction and thermal expansion

Magnetostriction (MS) is the $H$-induced change in the sample's dimensions at constant $T$. Thermal expansion (TE) is the change in the sample's dimensions as a function of $T$ at constant $H$. Both types of measurements were carried out with capacitance dilatometers made of copper.[43] The sensitivity for the fractional change in the length of the sample, $\Delta l/l$, was between $10^{-8}$ and $10^{-9}$. We shall use the unit vector $\hat{l}$ to specify the crystallographic direction along which the length $l$ was measured.

As discussed earlier,[44] the sample in our dilatometers is always subjected to a small uniaxial pressure exerted by the springs which hold it in place. In the present experiments, this uniaxial pressure was of order 30 bars (the exact value varied from run to run). The uniaxial pressure was always parallel to $\hat{l}$. Near the upper triple point, no noticeable dependence of the phase boundaries on the (small) uniaxial pressure was observed. However, a slight effect of the uniaxial pressure on the measured values of $T_C$ and $T_\alpha$ was expected, and will be discussed later.

The arrangement for controlling the temperature was as follows. The capacitance dilatometer containing the sample was surrounded by a copper can which contained helium exchange gas. This inner-copper can was surrounded by an outer-copper can, and the space between the two cans was evacuated ($P < 10^{-6}$ Torr). The entire arrangement was immersed in a cryogenic liquid. We used liquid helium, liquid nitrogen, or Freon 12, depending on the desired temperature. The thermal contact between the inner-copper can and the liquid bath was poor. The temperature of the inner can was controlled by a heater which was wound on the outer surface of this can. The heater worked against the small heat leak from the inner can to the bath. The temperature was either stabilized (in the MS measurements), or allowed to drift slowly (in the TE measurements).

Temperatures above 15 K were measured with a platinum resistance thermometer attached to the capacitance cell inside the inner can. The only data below 15 K were taken at 4.2 K, with helium exchange gas between the two cans and with a bath of liquid helium. Above 15 K, the small magnetoresistance of the platinum thermometer was corrected for when necessary. The precision of the temperature measurements in the important region between 77 and 150 K was 0.02 K, and the accuracy was 0.05 K. In other temperature regions, the precision and accuracy were better than 0.1 K, except for two data points near 15 K where the accuracy was 0.3 K.

Two magnets were used in the MS measurements: a NbTi superconducting magnet with a maximum field of 90 kOe, and a 12-in. O. S. Walker electromagnet with a maximum field of 20 kOe. The advantage of the superconducting magnet was the higher field. The advantage of the electromagnet was that it could be rotated so that the direction of $\vec{H}_0$ could be varied in one plane. The angular setting of the electromagnet would be read with a precision of 0.1°. The magnetic field of the superconducting magnet was known to an accuracy of 0.25%, and it was read with a precision of 1.4 Oe. The field of the electromagnet was known to an accuracy of 0.5%, and it was read with a precision of 1 Oe. The readability of the field was important because the data for $\Delta l$ vs $H_0$ were subsequently differentiated numerically with respect to $H_0$, to obtain $\partial l/\partial H_0$. The differentiation was performed on a small computer, using a linear-least-squares fit to data in a small field interval centered at the differentiation point.

All measurements of the TE were carried out in the electromagnet, keeping $\vec{H}_0$ constant during each measurement of $l$ vs $T$. The data were differentiated numerically with respect to $T$, to obtain $\partial l/\partial T$.

Because the primary purpose of the MS and TE measurements was to determine phase boundaries from anomalies in $\partial l/\partial H_0$ and $\partial l/\partial T$, no consistent attempt was made to measure the absolute magnitude of the change in length. Thus, most results for the fractional change in length, $\Delta l/l$, or the derivatives $\partial l/\partial H_0$ and $\partial l/\partial T$, will be expressed in arbitrary units. In the few instances in which the magnitude of $\Delta l/l$ was determined in the MS measurements, it

was found to be in rough agreement with the earlier data of Ishizaki *et al.*[22]

### D. Demagnetization corrections

In experiments with magnetic materials one must distinguish between the applied (external) magnetic field $\vec{H}_0$, and the internal magnetic field $\vec{H}$. The internal magnetic field is of greater fundamental significance, and is often the only magnetic field which is discussed in theoretical papers. Also, intrinsic susceptibilities such as $\bar{\chi}_{in}=M_H/H$ and $\chi^{\parallel}_{in}=\partial M_H/\partial H$ (i.e., average and differential parallel susceptibilities) are of greater theoretical significance than their measured counterparts $\bar{\chi}_m=M_H/H_0$ and $\chi^{\parallel}_m=\partial M_H/\partial H_0$. In ferromagnetic materials, such as MnP, the difference between $\vec{H}_0$ and $\vec{H}$, and the differences between intrinsic and measured $\chi$'s, can be important. To convert the measured quantities to intrinsic quantities one must apply demagnetization corrections. In the present work, such corrections were relatively unimportant in some cases, but crucial in others. The demagnetization corrections will be discussed in conjunction with the data analysis. In the present section we only quote some results which will be needed later.[45]

Consider an ellipsoidal sample of uniform composition, and assume that the principal axes of the ellipsoid form a coordinate system in which the intrinsic susceptibility tensor is diagonal. If a uniform $\vec{H}_0$ is applied along one of the principal axes then the magnetization $\vec{M}$ and the internal field $\vec{H}$ are uniform inside the sample, and are parallel to $\vec{H}_0$. The internal and applied fields are then related as

$$H=H_0-NM \quad , \tag{2}$$

where $N$ is the demagnetizing factor, which depends on the shape of the ellipsoid and on the direction of $\vec{H}_0$. The measured average susceptibility $\bar{\chi}_m=M/H_0$ is then related to the intrinsic average susceptibility $\bar{\chi}_{in}=M/H$ as

$$\bar{\chi}_m=\bar{\chi}_{in}/(1+N\bar{\chi}_{in}) \tag{3}$$

or

$$\bar{\chi}_m^{-1}=\bar{\chi}_{in}^{-1}+N \quad . \tag{4}$$

If $\bar{\chi}_{in}\gg 1/N$ then $\bar{\chi}_m\cong 1/N$. That is, $1/N$ is the upper limit for $\bar{\chi}_m$. The measured parallel differential susceptibility $\chi^{\parallel}_m$ also is related to its intrinsic counterpart $\chi^{\parallel}_{in}$ by Eqs. (2) and (3), with $\bar{\chi}$ replaced by $\chi^{\parallel}$. Let a small field $\vec{h}_0$ be applied perpendicular to $\vec{H}_0$, but parallel to one of the principal axes of the ellipsoid. Then $\chi^{\perp}_m=\partial M_h/\partial h_0$ is related to $\chi^{\perp}_{in}=\partial M_h/\partial h$ by the analogs of Eqs. (2) and (3), except that $N$ is the demagnetizing factor for the direction $\hat{h}_0$.

If a second-order magnetic phase transition occurs at $H=H(2)$, then the applied field at this transition is $H_0=H(2)+NM$, where $M$ is the magnetization at the transition.

Consider next a first-order magnetic phase transition which occurs at $H=H(1)$, with magnetizations just below and just above the transition equal to $M_1$ and $M_2$, respectively. As a function of applied field, the transition will commence at $H_0=H(1)+NM_1$, and will end at $H_0=H(1)+NM_2$. The transition will thus occur in a finite-field interval

$$\Delta H_0=N(M_2-M_1)\equiv N\Delta M \quad . \tag{5}$$

In this field interval the sample is in an intermediate "phase," which consists of a mixture of domains of the phases below and above the transition.

When the sample is not ellipsoidal, the situation is more complicated because $\vec{H}$ and $\vec{M}$ are not uniform inside the sample. Suppose that the material has a second-order phase transition which occurs when the magnitude of $\vec{H}$ is equal to $H(2)$, or when a particular component of $\vec{H}$ is equal to $H(2)$. The transition in different regions of the sample will then occur at different values of $\vec{H}_0$. If the transition is detected by measuring a property which is an integral over all regions of the sample (e.g., total magnetic moment, or the length of the sample) then the transition will appear rounded when measured as a function of $H_0$. In the case of a first-order transition, the values of $H_0$ where the transition starts and ends will not be sharply defined. In addition, the relation between the intrinsic and measured susceptibilities is more complicated than Eq. (3).

In spite of these difficulties for nonellipsoidal samples, it is still possible in many cases to obtain fairly accurate values for the internal transition fields and the intrinsic susceptibilities by making approximate demagnetization corrections. The approximate corrections are based on expressions for an ellipsoidal sample and on an average demagnetizing factor which is estimated from the shape of the sample.

## IV. PHASE DIAGRAM FOR $\vec{H}$ PARALLEL TO THE $b$ AXIS

### A. Global phase diagram

The global phase diagram (for $\vec{H}_0 \| b$) was determined from MS measurements on sample 3. The results are shown in Fig. 2. The phase diagram near the upper triple point (where the para, ferro, and fan phases meet) was also measured in samples 1 and 2. Although the focus of the present work is on the upper triple point, the transition at $T_\alpha$ and the phase boundary near $T_C$ will also be discussed. The lower triple point (where the ferro, fan, and screw phases meet) was carefully investigated by Ishizaki *et al.*[22] Our own data near this point are consistent with theirs, and will not be described here. However, we note that all existing data for the lower triple point indicate that it is an ordinary triple point (not a multicritical point).

### B. Screw-ferro transition at $T_\alpha$

The screw-ferro transition at $T_\alpha$ was determined from thermal expansion data on sample 3. The measurements were performed at $H=0$, with $\hat{l} \parallel b$. A uniaxial pressure of $49 \pm 10$ bars was present during the measurements (see Sec. III C). The transition at $T_\alpha$ was of first order, and exhibited a hysteresis.[46] The width of the transition was approximately 0.5 K, and the hysteresis was approximately 0.24 K. The temperatures at the center of the transition, averaged for increasing and decreasing $T$'s, was $T_\alpha = 45.5 \pm 0.1$ K.

The transition at $T_\alpha$ is known to depend on uniaxial pressure.[36] Correcting for this dependence, we obtain $T_\alpha = 45.8$ K at zero stress. This value is comparable to other published values, although most other values are higher by 1–6 K. Recent work indicates that $T_\alpha$ depends on sample purity, and that this dependence can be as large as several degrees K.[26]

The screw-to-ferro transition at $T_\alpha$ is accompanied by a jump $\delta l_b$ in the length of the sample along the $b$ direction. Our data indicate that $\delta l_b$ is negative. In contrast, Refs. 19 and 20 show a positive $\delta l_b$. We believe our sign to be correct, for the following reasons: (i) The screw-to-ferro transition is accompanied by an increase in entropy. The derivative of $T_\alpha$ with respect to a uniaxial pressure along $b$ is negative.[36] Therefore, the analog of the Clapeyron-Clausius equation gives a negative $\delta l_b$. (ii) The screw-to-ferro transition occurs also in finite $H$, where it can be observed in MS measurements. Both our data and those in Ref. 22 show that this transition is accompanied by a decrease in the $b$ dimension.

### C. Para-ferro phase boundary near $T_C$

#### 1. *Magnetostriction and thermal expansion data*

The para-ferro boundary in the $TH$ plane (and for $\vec{H} \parallel b$) will be designated as either $T_\lambda(H)$ or $H_\lambda(T)$. In the $TH_0$ plane, this phase boundary will be designated as $T_\lambda(H_0)$ or $H_{0\lambda}(T)$. This phase boundary was determined from TE (thermal expansion) and MS (magnetostriction) measurements. The method was based on the expectation that the order-disorder transition would be accompanied by $\lambda$ anomalies in the second derivatives of the thermodynamic potential $\Phi(T,H,P)$. This potential is the analog of the Gibbs potential. Because the volume $V$ is equal to $\partial\Phi/\partial P$, the derivatives $\partial V/\partial T$ and $\partial V/\partial H$ should exhibit $\lambda$ anomalies at the transition. One can also consider a thermodynamic potential which involves a uniaxial pressure instead of the hydrostatic pressure $P$. Then one expects $\lambda$ anomalies in the $T$ and $H$ derivatives of the sample's length $l$. This was confirmed by our experiments. In the TE data, the para-ferro transition appeared as a $\lambda$ anomaly in $\partial l/\partial T$ vs $T$, measured at a constant $H_0$. The temperature at the anomaly was chosen as $T_\lambda(H_0)$. In the MS data, the para-ferro transition appeared as a $\lambda$ anomaly in $(\partial l/\partial H_0)_T$ vs $H_0$. The magnetic field at the anomaly (defined more precisely later) was chosen as $H_{0\lambda}(T)$.

All TE data were taken with $\hat{l} \parallel b$. The results at $H_0 = 0$ were similar to those obtained earlier.[19–21] For nonzero $H_0$, the $\lambda$ anomaly in $\partial l/\partial T$ decreased in magnitude as $H_0$ increased. As a result, only data at relatively low fields ($H_0 \lesssim 4$ kOe) could be used to determine $T_\lambda(H_0)$. In contrast, the para-ferro transition was easily obtained from MS measurements. These measurements gave $H_{0\lambda}(T)$ for all $T$'s except when $(T_C - T) \lesssim 0.5$ K.

Figure 3 shows examples of MS data at 283.8 and 292.8 K. These data are for $\hat{l} \parallel b$. At the lower temperature, which is below $T_C$, there is a rounded peak which is related to the ferro-para transition. (This rounded peak of $\Delta l/l$ should not be confused with the sharper $\lambda$ peak of $\partial l/\partial H_0$ that is discussed later.) The magnitude of the peak of $\Delta l/l$ in Fig. 3 is roughly $5 \times 10^{-6}$. The MS data for 292.8 K, which is above $T_C$, are monotonic in $H_0$, and show no distinct feature which can be associated with a phase transition.

The MS data at 283.8 K were differentiated numerically, to obtain $\partial l/\partial H_0$. The results are shown in

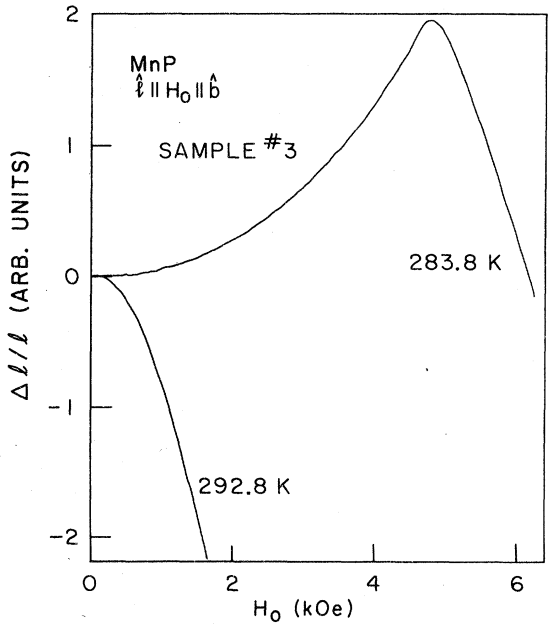


FIG. 3. Longitudinal magnetostriction, with $\vec{H}_0 \parallel b$, at 283.8 and 292.8 K. Here, $\vec{H}_0$ is the applied magnetic field, and $\Delta l/l$ is the fractional change in the sample's length $l$. The unit vector $\hat{l}$ specifies the crystallographic direction along which the change in length is measured.

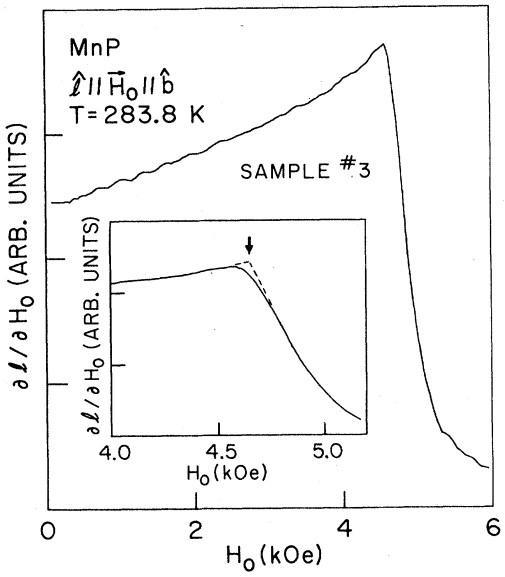


FIG. 4. Derivative of the length $l$ with respect to $H_0$ at 283.8 K, as obtained by numerical differentiation of the data in Fig. 3. The inset shows our choice for the transition field $H_{0\lambda}$, which is indicated by an arrow.

Fig. 4. It is obvious that the magnetic transition is accompanied by a $\lambda$ anomaly in $\partial l/\partial H_0$. Our choice for the transition field $H_{0\lambda}$ is illustrated in the inset of Fig. 4; tangents are drawn at the inflection points on both sides of the maximum, and the intersection of these tangents is chosen at $H_{0\lambda}$. This method was preferable to choosing the field at the maximum of $\partial l/\partial H_0$ as $H_{0\lambda}$ because: (1) the exact location of the maximum was harder to determine in some cases, and (2) the location of the maximum was slightly affected by the differentiation procedure. (The derivative $\partial l/\partial H_0$ was obtained from a linear fit over a small interval $\Delta H_0$. The field at the maximum of $\partial l/\partial H_0$ depended slightly on the magnitude of $\Delta H_0$, whereas the field defined in the inset of Fig. 4 was very nearly independent of $\Delta H_0$, for a small $\Delta H_0$.) In analyzing the TE data, we chose $T_\lambda$ in a manner analogous to our choice for $H_{0\lambda}$.

Some MS data were also taken with $\hat{l} \| c$, instead of $\hat{l} \| b$. These data were obtained mostly at $T$'s well below $T_C$. Figure 5 shows the results at two temperatures: one below $T_C$, and another above $T_C$. A comparison with Fig. 3 shows that near $T_C$ the sign of the MS for $\hat{l} \| c$ is opposite to that for $\hat{l} \| b$. In Fig. 5, the minimum value of $\Delta l/l$, for $T = 265.4$ K, is of order $-1 \times 10^{-5}$.

### 2. *Phase boundary*

The para-ferro phase boundary near $T_C$ is shown in Fig. 6. The ordinate is $H_0^2$. Just below $T_C$, the transition temperature $T_\lambda(H_0)$ is linear in $H_0^2$, with a slope $dT_\lambda/d(H_0^2) = -0.3$ K kOe$^{-2}$. Demagnetization corrections for this slope were made using the susceptibility data in Ref. 16, and the estimate $N_b \cong 2.3$ for the effective demagnetizing factor associated with the $b$ direction of sample 3. This gave $H = 0.9 H_0$ near $T_C$, which implied that $dT_\lambda/d(H^2)$ was roughly 23% higher than $dT_\lambda/d(H_0^2)$. Because the sample was not ellipsoidal, this demagnetization correction is only a rough estimate.

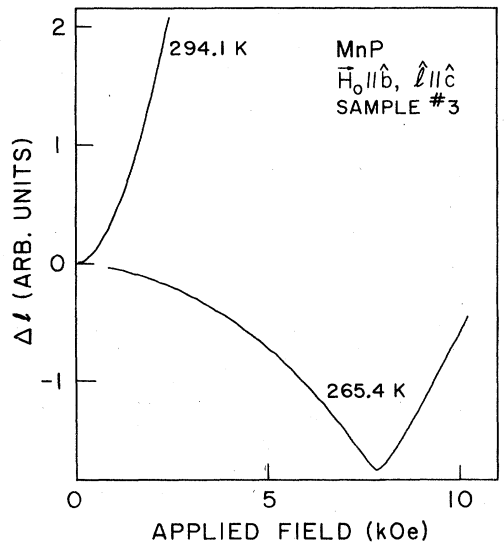


FIG. 5. Transverse magnetostriction at 265.4 and 294.1 K, measured with $\vec{H}_0 \| b$ and $\hat{l} \| c$.

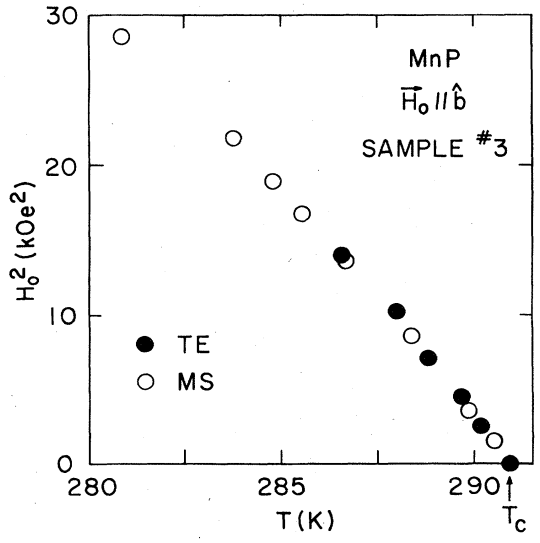


FIG. 6. Para-ferro phase boundary near $T_C$. These results were obtained from magnetostriction (MS) and thermal expansion (TE) measurements with $\hat{l} \| \vec{H}_0 \| b$.

The Curie temperature obtained from our TE data was 290.9 ±0.1 K. However, as in the case of $T_a$, this value must be corrected for the effect of the uniaxial pressure ($p \cong 49$ bars). Using the data in Ref. 36, we estimate that the uniaxial pressure increased $T_C$ by 0.05 K. Thus, $T_C = 290.85 \pm 0.1$ K for sample 3 at zero stress. This value agrees with published values, which range from 290.5 to 291.5 K.

### 3. *Thermal scaling axis*

The main purpose of the following paragraphs is to facilitate a later discussion of scaling axes near the upper triple point.

The phase diagram of an anisotropic ferromagnet was considered theoretically by Riedel and Wegner.[47] Their discussion includes the case when: (1) there is a unique easy axis, (2) the hard axes are perpendicular to the easy axis, and (3) $\vec{H}$ is in a plane which contains the easy axis and a hard axis. The results for this case were recently used to interpret experimental data in $NiZrF_6 \cdot 6H_2O$.[48] Here we use these results to interpret the para-ferro phase boundary of MnP.

The phase diagram expected from the theory of Riedel and Wegner is shown in Fig. 7. To facilitate the comparison with the data in MnP, we have identified the easy axis as the $c$ axis, and the hard axis as the $b$ axis. When $H_b = H_c = 0$, the transition occurs at the Curie temperature $T_C = T_\lambda(0)$. For a finite $H_b$ (and $H_c = 0$), the transition occurs at $T_\lambda(H_b)$. The locus of the points $T_\lambda(H_b)$ is a λ line of second-order phase transitions. This line is in the $TH_b$ plane. No phase transition is expected in the presence of a finite ordering field $H_c$. For small $H_b$, the difference $(T_C - T_\lambda)$ should be proportional to $H_b^2$. This last prediction agrees with the results in MnP (see Fig. 6).

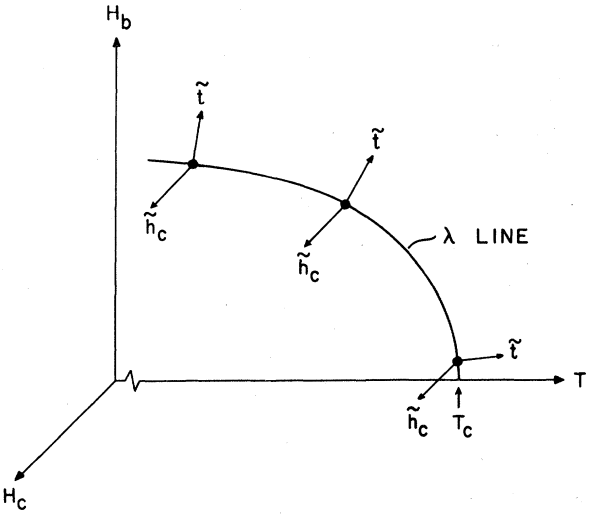


FIG. 7. Schematic of the expected phase diagram of MnP at temperatures well above the upper triple point. This figure is based mainly on the theory in Ref. 47. The scaling axes $\tilde{t}$ and $\tilde{h}_c$ at several points on the λ line (para-ferro line) are indicated.

The critical behavior on the λ line is expected to be Ising-like because the order parameter $M_c$ has a single component. When $H = 0$, one has the familiar case in which: (1) $M_c$ is proportional to $(T_c - T)^\beta$ for $T$ just below $T_C$, and (2) $\partial M_c/\partial H_c$ is proportional to $(T - T_C)^{-\gamma}$ for $T$ just above $T_C$. The available experimental data for the critical exponents of MnP, at $H = 0$, are in fair agreement with these predictions.[16] The small deviations from Ising exponents are presumably attributable to residual crossover effects from Heisenberg (or $XY$) to Ising behaviors. Such a crossover is expected as $T$ approaches $T_C$.

The scaling assumption made by Riedel and Wegner is that the singular part of the thermodynamic potential, near the λ line, depends on two scaling variables: (i) the ordering-field variable $\tilde{h}_c$, which is proportional to $H_c$ (but with a proportionality constant which may depend on $H_b$ and $T$), and (ii) a thermal variable $\tilde{t}$ that measures the "distance," in the $TH_b$ plane, from the λ line. When $H_b = 0$, the variable $\tilde{t}$ is the familiar thermal variable, which is proportional to $(T - T_C)$. Then, one has relations such as $M_c \propto |\tilde{t}|^\beta$ and $\partial M_c/\partial H_c \propto \tilde{t}^{-\gamma}$ for the critical behavior on the $T$ axis.

For a finite $H_b$, the scaling axis $\tilde{t}$ is no longer parallel to the $T$ axis. This is illustrated in Fig. 7. In particular, for $T \ll T_C$ (where the λ line is nearly parallel to the $T$ axis), the $\tilde{t}$ axis which is expected from Ref. 47 is nearly parallel to the $H_b$ axis. Then, to a good approximation, $\tilde{t}$ is proportional to $H_b - H_\lambda(T)$. Thus, at $T \ll T_C$, one expects that the critical behavior in the $TH_b$ plane will be governed by relations such as $M_c \propto [H_\lambda(T) - H_b]^\beta$ and $\partial M_c/\partial H_c \propto [H_b - H_\lambda(T)]^{-\gamma}$.

The preceding discussion, which was based on the early work of Riedel and Wegner, must be modified in light of more recent theoretical developments. Within the scaling theory, the direction of the $\tilde{t}$ axis is not uniquely determined. At a given point on the λ line, the direction of the $\tilde{t}$ axis can be chosen to be parallel to any direction in the $TH_b$ plane, with the exception of the direction of the tangent to the λ line.[49,50] All such nontangent directions will lead to the same asymptotic critical behavior (i.e., very close to the λ line). However, the range of validity of the scaling laws will depend on the choice of the $\tilde{t}$ axis. An optimal choice for $\tilde{t}$ will maximize the range over which the scaling laws are obeyed. Such an optimal scaling axis is, in principle, obtainable from a renormalization-group calculation by eliminating the appropriate redundant eigenoperators.[51] In the absence of such a calculation, the optimal choice for $\tilde{t}$ is not known, except at the Curie point where the sym-

metry with respect to reversal of $H_b$ selects the $T$ axis as the optimal direction. As far as we know, the optimal thermal axis for the present problem has not been calculated. Nevertheless, we expect that for $T \ll T_C$, the choice of the $\tilde{t}$ axis as parallel to the $H_b$ axis will lead to a comparatively wide range over which the scaling laws will be obeyed. In any case, such a choice for the thermal scaling axis will certainly lead to the correct asymptotic critical behavior.

Finally, it should be remarked that all scaling axes considered in the present paper are linear scaling axes.

### D. Phase boundaries near the upper triple point

#### *1. Phase boundaries from parallel differential susceptibility in sample 1*

The parallel differential susceptibility was measured in sample 1, with $\vec{H}_0 \| b$. Figure 8 shows several traces of $\chi_m^{\|} = \partial M_b/\partial H_0$ vs $H_0$, taken at different temperatures. Curve a, for $T = 123$ K, is typical for temperatures above 121 K. At these temperatures the sample is in the ferro phase when $H_0 < H_{0\lambda}$, and in the para phase when $H_0 > H_{0\lambda}$. In the ferro phase, $\chi_m^{\|}$ is positive and is nearly independent of $H_0$. The positive $\chi_m^{\|}$ corresponds to an increase of $M_b$ with increasing $H_0$ (in the ferro phase). This is attributed to the rotation of the magnetization in a single ferromagnetic domain toward the direction of $\vec{H}_0$. This rotation is completed when $H_0$ reaches $H_{0\lambda}$. Thus, the ferro-to-para transition is marked by a rapid decrease of $\chi_m^{\|}$ with increasing $H_0$, which leads to a "shoulder" in the susceptibility curve. The transition field $H_{0\lambda}$ was chosen as the intersection of a tangent drawn at a field just below the shoulder with the tangent at the inflection point just above the shoulder.

The curves b–d in Fig. 8 are for temperatures below 121 K. Each of these curves exhibits a sharp peak at $H_0 = H_{01}$, and a "shoulder" at a higher field $H_{0\lambda}^*$. The field $H_{01}$ is identified as the ferro-fan transition field. The field $H_{0\lambda}^*$ is identified as the fan-para transition field. Our method for choosing $H_{0\lambda}^*$ is illustrated in the inset of Fig. 8, and is similar to that in the inset of Fig. 4.

Figure 9 shows the phase boundaries obtained from the data for $\chi_m^{\|}$, taken on sample 1. Also shown in this figure are the phase boundaries obtained from the MS data on sample 2, which are discussed in Sec. IV D 2. Note that the ordinate is the applied magnetic field. The demagnetization corrections will be discussed later. Figure 10 shows an expanded view of the results in sample 1 for temperatures near the upper triple point.

Besides the transition fields, some other features of the susceptibility data are noteworthy: (i) The value of $\chi_m^{\|}$ in the ferro phase is nearly independent of $H_0$ and of $T$, for $80 < T < 150$ K. (ii) For a fixed $T$

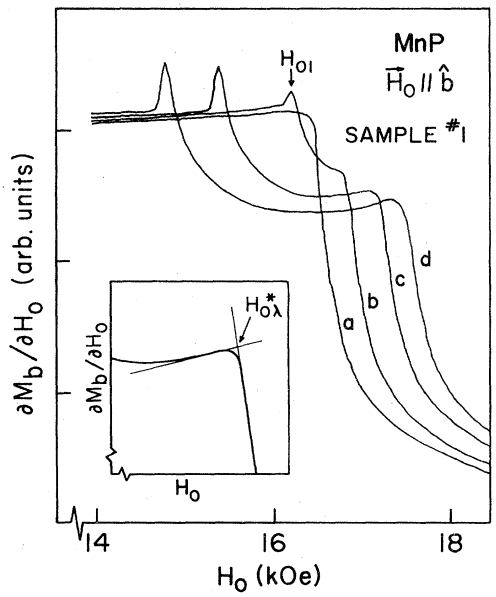


FIG. 8. Dependence of the measured parallel differential susceptibility $\partial M_b/\partial H_0$ on applied magnetic field $H_0$. The four curves are for a, $T = 123.0$ K; b, $T = 113.8$ K; c, $T = 107.6$ K; and d, $T = 104.0$ K. The inset shows our choice for the transition field $H_{0\lambda}^*$.

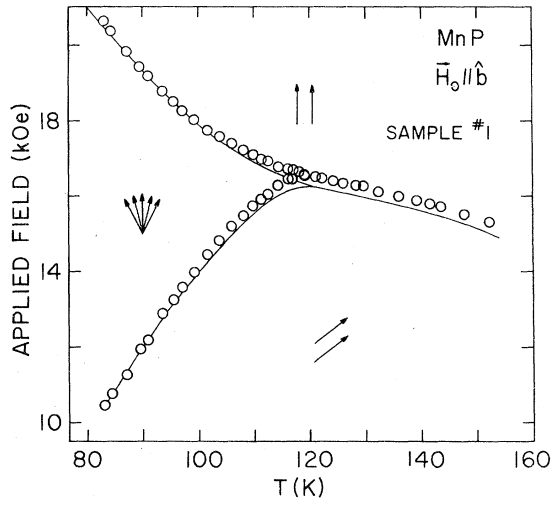


FIG. 9. Phase diagram near the upper triple point. The experimental points are from parallel differential susceptibility data on sample 1. Some additional experimental points were deleted, to avoid overcrowding. The solid curves are the smoothed results for sample 2, which were obtained from magnetostriction data, and which are shown here for comparison.

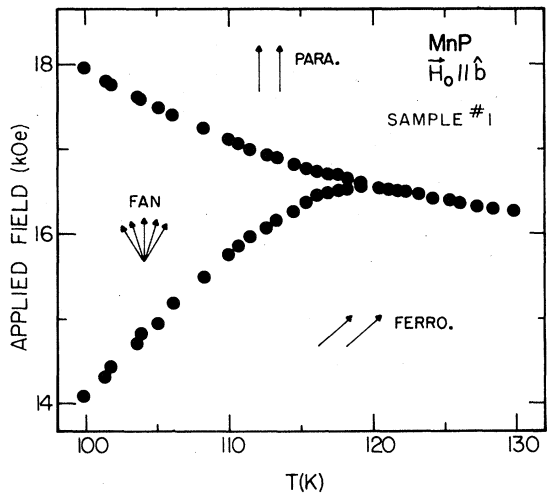


FIG. 10. Expanded view of the phase diagram of sample 1 near the upper triple point.

below 121 K, the susceptibility $\chi_m^{\|}$ in the fan phase is lower than that in the ferro phase, and it decreases with increasing $H_0$ (except for a slight increase just below $H_{0\lambda}^*$). (iii) For a given $H_0$, the susceptibility $\chi_m^{\|}$ in the fan phase increases with increasing $T$.

### 2. *Phase boundaries from MS data for sample 2*

Magnetostriction measurements on sample 2 were performed between 77 and 152 K. Data were taken for two experimental configurations: (1) the longitudinal configuration, $\vec{H}_0 \| \hat{l} \| b$, and (2) the transverse configuration, $\vec{H}_0 \| b$ and $\hat{l} \| c$. The data for the longitudinal configuration were taken in a superconducting magnet (maximum field = 90 kOe). In the transverse configuration, the magnetic field was produced by an electromagnet (maximum field is equal to 20 kOe).

Examples of MS data for $T < 121$ K are shown in Figs. 11(a) and 12(a). Part (b) of each of these figures shows the corresponding derivative $\partial l/\partial H_0$. The ferro-fan transition at $H_{01}$ is clearly identified by the sharp spike in $\partial l/\partial H_0$. This spike is positive for

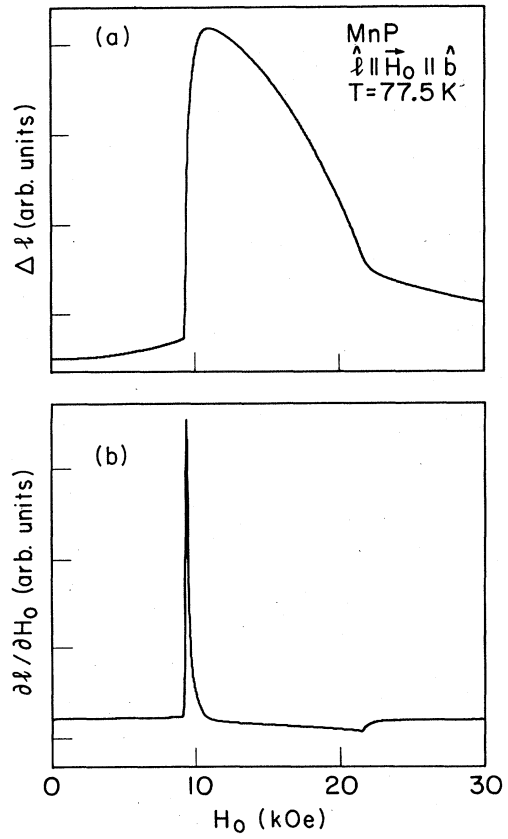


FIG. 11. (a) Longitudinal magnetostriction $\Delta l$ of sample 2, measured at 77.5 K with $\vec{H}_0$ parallel to the $b$ axis. (b) The derivative $\partial l/\partial H_0$ obtained from part (a).

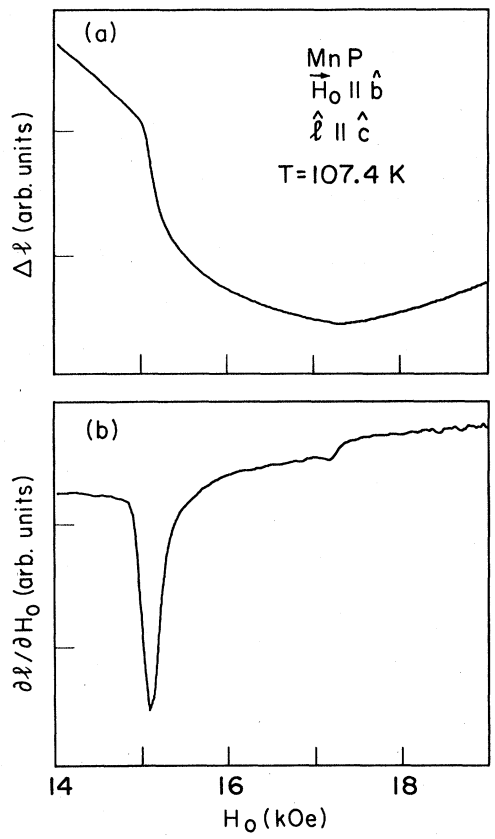


FIG. 12. (a) Transverse magnetostriction $\Delta l$ of sample 2, measured at 107.4 K with $\vec{H}_0 \| b$ and $\hat{l} \| c$. (b) The derivative $\partial l/\partial H_0$ obtained from part (a).

the longitudinal configuration, and negative for the transverse configuration. The fan-para transition, at $H_{0\lambda}^{*}$, is marked by a $\lambda$ anomaly in $\partial l/\partial H_0$ vs $H_0$. Our choice of $H_{0\lambda}^{*}$ was similar to that in the inset of Fig. 4.

At temperatures well below 121 K, the transition fields $H_{01}$ and $H_{0\lambda}^{*}$ were well separated from each other. The two transitions were then easily resolved, even though the magnitude of the $\lambda$ anomaly at $H_{0\lambda}^{*}$ was small in comparison with the spike at $H_{01}$. However, for $T$ not far below 121 K, the two transitions were close to each other, and the $\lambda$ anomaly was less readily resolved. One advantage of the transverse configuration ($\hat{l} \parallel c$) was that the $\lambda$ anomaly was resolved even at $T$'s which were close to 121 K. This was not the case for the longitudinal configuration.

An example of MS data above 121 K is shown in Fig. 13(a). Figure 13(b) shows the corresponding derivative $\partial l/\partial H_0$. This derivative exhibits a $\lambda$ anomaly at the ferro-para transition. The transition field $H_{0\lambda}$ was chosen as in the inset of Fig. 4.

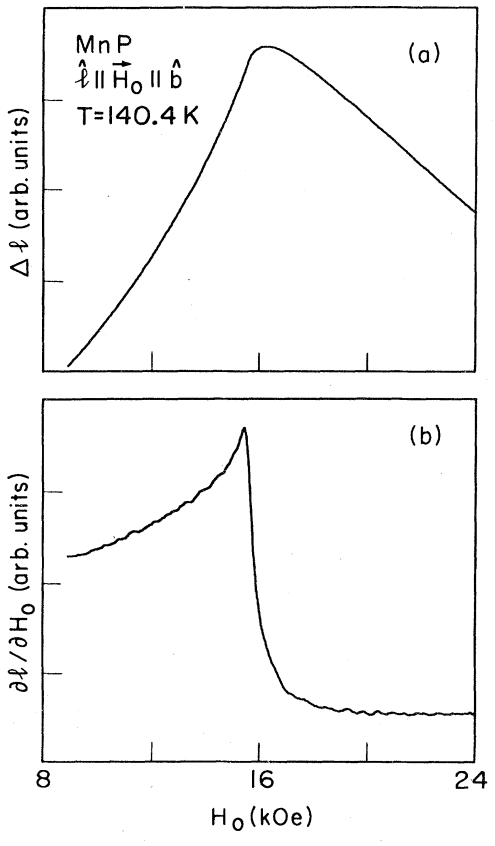


FIG. 13. (a) Longitudinal magnetostriction $\Delta l$ of sample 2, measured at 140.4 K with $\vec{H}_0$ parallel to the $b$ axis. (b) The derivative $\partial l/\partial H_0$ obtained from part (a).

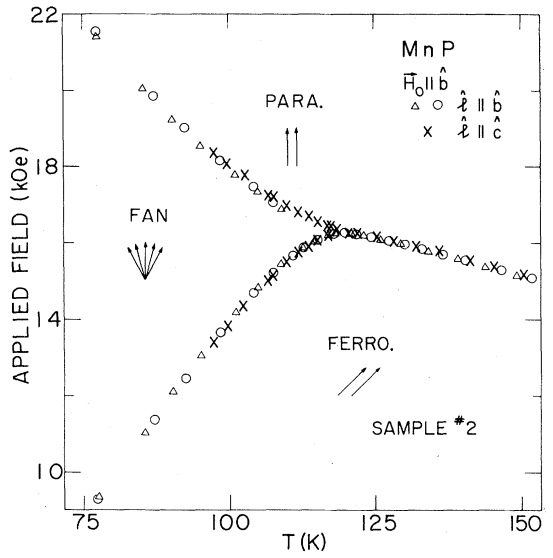


FIG. 14. Phase diagram of sample 2 near the upper triple point. These results were obtained from MS measurements with $\vec{H}_0 \parallel b$, and with $\hat{l}$ parallel to either $b$ or $c$.

The phase diagram obtained from the MS data in sample 2 is shown in Fig. 14. An expanded view of the results near the upper triple point is shown in Fig. 15. A still more expanded version of the phase diagram (not shown) indicates that the temperature at this triple point is $T_t = 121 \pm 1$ K.

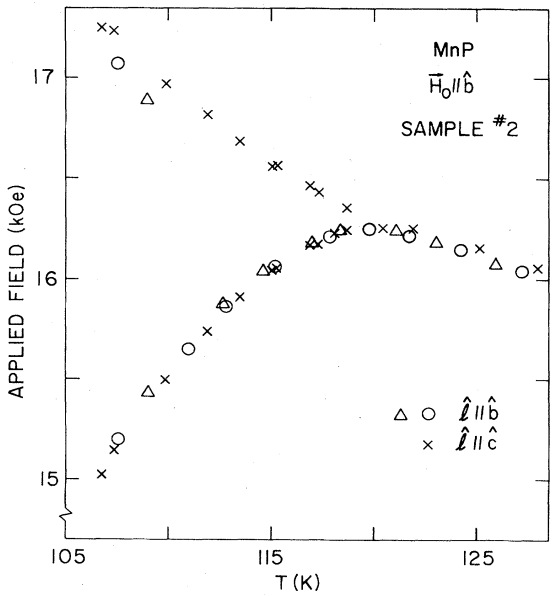


FIG. 15. Expanded view of Fig. 14 near the upper triple point.

### 3. *Phase boundaries from MS data for sample 3*

The global phase diagram for sample 3, as obtained from MS data, is shown in Fig. 2. Figure 16 shows an expanded view of these results near the upper triple point. For comparison, the results for samples 1 and 2 are also indicated in this figure. Note, however, that none of the results in Fig. 16 were corrected for demagnetization effects, and that these corrections are slightly different for different samples. The demagnetization corrections are discussed in Sec. IV D 4.

### 4. *Demagnetization corrections*

The demagnetization correction depends on the intrinsic susceptibility and the demagnetizing factor. Consider the ferro phase and assume that $\vec{H}_0$ is parallel to $b$. For $50 < T < 108$ K, the intrinsic susceptibility $\bar{\chi}_b = M_b/H_b$ is nearly a constant, and is approximately $2.2 \times 10^{-2}$ emu (Refs. 14 and 15). Our own data for the ferro phase show that $\bar{\chi}_b$ is also nearly constant between 108 and 150 K. In the fan phase, $\bar{\chi}_b$ is not a constant. Nevertheless, between 77 and 150 K this susceptibility varies only between $2.2 \times 10^{-2}$ and $2.6 \times 10^{-2}$ emu approximately.[15] Thus, the values of $\bar{\chi}_b$ do not vary greatly on the phase boundaries in Figs. 8, 9, and 14–16.

Using the physical dimensions of our samples, we obtained the following rough estimates for the demagnetizing factor: $N_b \cong 1$ for sample 1, $N_b \cong 1.3$ for sample 2, and $N_b \cong 2.3$ for sample 3. As a check, we also estimated $N_b$ from the width $\Delta H_0$ of the screw-fan transition at 4.2 K. Here, we assumed that $\Delta H_0$ was caused by demagnetization effects. Using Eq. (5) and the known magnetization discontinuity $\Delta M$, we obtained $N_b \cong 1.2$ for sample 2 and $N_b \cong 2.1$ for sample 3.

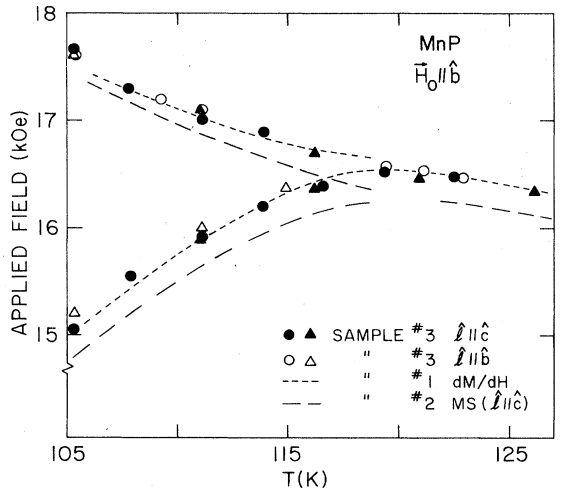


FIG. 16. Phase diagram of sample 3 near the upper triple point, as obtained from MS measurements with $\hat{l} \| b$ or $\hat{l} \| c$. Also shown are the smoothed results for sample 1 (obtained from susceptibility data), and for sample 2 (obtained from the MS data with $\hat{l} \| c$).

Using these numbers and Eq. (2) we estimated that for $77 < T < 150$ K, the internal magnetic fields $H_1$, $H_\lambda^*$, and $H_\lambda$ were lower than the corresponding applied fields by 2–3% for samples 1 and 2 and 5–6% for sample 3. These demagnetization corrections are relatively small. Also, although the demagnetization correction (expressed as a percentage of the applied field) is not a constant for a given sample, its variation is small in the *TH* region of interest.

The demagnetization corrections account for most of the difference between the *applied* transition fields in samples 2 and 3 (see Fig. 16). These samples were measured in the same laboratory using the same technique (magnetostriction). However, the applied transition fields for sample 1 are 2–3% higher than expected from the results in the other two samples and the different demagnetizing factors. This discrepancy might have been caused by different field calibrations in the two laboratories, and by the different experimental techniques which were used.

### 5. *Field misalignment*

Near the upper triple point, the results for $H_{0\lambda}^*$ and $H_{0\lambda}$ are sensitive to small deviations of the direction of $\vec{H}_0$ from the $b$ axis (see Sec. VI). More specifically, the results are sensitive to the presence of a small $c$ component of $\vec{H}_0$, but are insensitive to the presence of a small $a$ component. A misalignment of, say, 2° in the $bc$ plane can be important, whereas a similar misalignment in the $ab$ plane is not. The strong dependence of some of the phase boundaries on $H_{0c}$ ($c$ component of $\vec{H}_0$) was not discovered until after the data in samples 1 and 2 had already been taken. The direction of $\vec{H}_0$ in the experiments with these two samples was known only to within 2°. The field alignment in the experiments with sample 3 was much more careful. In the present section we discuss the field alignment for sample 3, and also the possible errors which a field misalignment might have caused in the data for samples 1 and 2.

In those measurements with sample 3 that were made below 20 kOe, the field misalignment in the $bc$ plane was less than 0.2°. As shown in Sec. VI, such a small misalignment had a negligible effect on the results. Therefore, the data for sample 3 that are shown in Fig. 16 are free from misalignment errors.

Those data for sample 3 that were obtained above 20 kOe, were taken in a superconducting magnet. Initially, the alignment was known only to within 2°. However, by repeating some of the measurements below 20 kOe, and comparing the results with the measured dependence on misalignment (Sec. VI), it

was concluded that the actual misalignment in the *bc* plane was less than 0.5°. On the basis of the trends observed below 20 kOe, we expect that such a small misalignment did not have any noticeable effect on the results above 20 kOe. Thus, all the data in Fig. 2, for the global phase diagram, are practically free from misalignment errors.

As discussed later, a field misalignment (in the *bc* plane) lowers the measured value of $H_{0\lambda}^{*}$, but does not affect $H_{01}$. Thus, the misalignment decreases the difference $(H_{0\lambda}^{*}-H_{01})$, measured at the same $T$. In addition to changing some of the transition fields, the misalignment also broadens the second-order phase transitions at $H_{0\lambda}$ and $H_{0\lambda}^{*}$, and makes the transition at $H_{01}$ less pronounced. When the misalignment in the *bc* plane is large enough, these transitions disappear altogether.

Consider Fig. 16. A comparison between the results for sample 1 with those for sample 3 shows no systematic differences. In particular, values of $[H_{0\lambda}^{*}(T)-H_{01}(T)]$ for these two samples are very nearly the same. We, therefore, conclude that the effects of field misalignment on the results for sample 1 were negligible.

For sample 2, one has to distinguish between the data with $\hat{l} \parallel c$ and those with $\hat{l} \parallel b$, because they correspond to different settings of $\vec{H}_0$. In Fig. 16, the data for $\hat{l} \parallel c$ are compared with those for sample 3. For $T$ above 110 K, the boundaries $H_{0\lambda}^{*}(T)$ and $H_{01}(T)$ for sample 2 have slightly different shapes than those for sample 3. However, the difference $[H_{0\lambda}^{*}(T)-H_{01}(T)]$ is nearly the same for both samples (it is actually slightly larger for sample 2). Based on the fact that $(H_{0\lambda}^{*}-H_{01})$ decreases when $\vec{H}_0$ is misaligned in the *bc* plane, we believe that the data for sample 2 (with $\hat{l} \parallel c$) were not affected significantly by misalignment.

Those data for sample 2 that were taken with $\hat{l} \parallel b$ gave slightly lower values for $(H_{0\lambda}^{*}-H_{01})$ than those taken with $\hat{l} \parallel c$. The clearest example of this difference is shown in Fig. 15. In this figure, $H_{01}$ is practically the same for $\hat{l} \parallel b$ and $\hat{l} \parallel c$, but $H_{0\lambda}^{*}$ is approximately 0.15 kOe lower for $\hat{l} \parallel b$. It is likely that the lower $H_{0\lambda}^{*}$ was caused by a small misalignment in the *bc* plane. However, other explanations of a difference as small as 0.15 kOe are also possible.

The preceding comparisons suggest that the errors caused by field misalignment were negligible in all cases, except for the results for sample 2 with $\hat{l} \parallel b$. In the latter case, the misalignment errors (if any) were still quite small. An explanation as to why the misalignment errors in samples 1 and 2 were so small can be given in terms of the demagnetizing factors, as follows.

The error in $H_{0\lambda}^{*}$ that is caused by a fixed angular misalignment of $\vec{H}_0$ (in the *bc* plane) depends on the demagnetizing factor $N_c$ (see Sec. VI A 2). The larger is $N_c$, the smaller is the error. In our experiments, the physical dimensions of samples 1 and 2 were such that $N_c$ was comparatively large, for either sample. The estimated values are $N_c \cong 10$ for sample 1, and $N_c \cong 6$ for sample 2, which should be compared with $N_c \cong 2$ for sample 3. The large demagnetizing factors for samples 1 and 2 should have reduced the sensitivity to misalignment, as compared with the sensitivity of sample 3 that is discussed in Sec. VI.

## V. DISCUSSION OF THE PHASE DIAGRAM NEAR THE UPPER TRIPLE POINT

The main question which we address in this paper is whether the upper triple point of MnP is a LP. In the present section we show that the phase diagram provides evidence that the triple point is indeed a LP. We shall first focus on the qualitative features of the phase diagram. A quantitative analysis, in terms of a crossover exponent, will be given later.

### A. Qualitative features

The upper triple point is clearly a point where paramagnetic, ferromagnetic, and helicoidal (fan) phases meet. This is one of the basic features of a LP. The susceptibility and MS results indicate that the para-ferro and para-fan transitions are of second order, which is another basic feature of a LP.

As shown by Hornreich,[8] a ferromagnetic LP in an orthorhombic crystal, such as MnP, should be characterized by $d=3$, $n=m=1$. The known properties of MnP are consistent with this prediction. The material has a unique easy axis ($n=1$), which is the $c$ axis. The wave vector $\vec{q}$ in the fan phase has only a single component ($m=1$), which is parallel to the $a$ axis.

The phase boundaries near a LP with $d=3$, $n=m=1$, were calculated using a Landau-type theory,[52] and also from high-temperature series expansions.[5] The Landau-type calculation is for all phase boundaries, including the ferro-helicoidal boundary. The series calculation is only for the two segments of the $\lambda$ line, namely, the para-ferro and para-helicoidal segments. Both calculations show that the two segments of the $\lambda$ line are tangent to each other at the LP. The Landau-type calculation shows that the ferro-helicoidal transition is of first order, and that the line of these transitions is tangent to the $\lambda$ line at the LP. The series calculation indicates that the $\lambda$ line has an inflection point at the LP. Our experimental results for the shapes of the phase boundaries near the upper triple point show all these expected qualitative features. We also find that the ferro-fan transition is of first order, as predicted. Thus, the qualitative features of the data are consistent with a LP.

### B. Crossover exponent

To analyze the data quantitatively, we assume that the upper triple point is a multicritical point, which obeys generalized scaling. Under this assumption, the shape of each of the two segments of the $\lambda$ line (in the $TH_b$ plane, and near the triple point) is described by a crossover exponent $\phi$. The assumption of generalized scaling (near the triple point) is expected to remain valid at the ferro-fan boundary. Then the shape of the boundary $H_1(T)$ is also governed by the same crossover exponent. Our purpose is to obtain $\phi$ from the data, and to compare it with the predicted value for a LP.

#### *1. Scaling axes*

We confine our attention to the $TH_b$ plane, and introduce two linear scaling axes using the usual procedure near a multicritical point.[50,53,54] We choose one scaling axis, $\bar{p}$, tangent to the phase boundaries at the triple point. The second scaling axis, $\bar{t}$, can be taken along any direction which is not tangent to the phase boundaries. That is, any nontangent direction will lead to the same asymptotic critical behavior. An optimal choice for the $\bar{t}$ axis does exist, as discussed by Fisher for the case of a bicritical point.[54] However, this optimal choice is not known for the present case. For convenience, we choose the $\bar{t}$ axis parallel to the $H_b$ axis. The scaling axes are shown in Fig. 17(a). Under the assumptions made, the shape of each of the phase boundaries $H_\lambda^*(T)$, $H_\lambda(T)$, and $H_1(T)$ near the triple point is given by

$$\bar{t}=\text{const}|\bar{p}|^{1/\phi} \ . \tag{6}$$

Expressing $\bar{t}$ and $\bar{p}$ in terms of $H_b$ and $T$, the following asymptotic forms for the phase boundaries near the triple point are obtained:

$$H_\lambda^*-H_t=A(T_t-T)+B_1(T_t-T)^{1/\phi} \ , \tag{7}$$

$$H_\lambda-H_t=-A(T-T_t)+B_2(T-T_t)^{1/\phi} \ , \tag{8}$$

and

$$H_1-H_t=A(T_t-T)+B_3(T_t-T)^{1/\phi} \ , \tag{9}$$

where $(T_t,H_t)$ is the upper triple point, $A$ is the negative slope, $-dH_b/dT$, of the tangent at the triple point, and $B_i$ are constants.

In principle, one can fit the phase boundaries to Eqs. (7)–(9), and thereby obtain $A$, $B_i$, $\phi$, $T_t$, and $H_t$. In practice, we could not obtain reliable values when all these parameters were allowed to vary in the least-squares fits. Because our main objective was to obtain $\phi$, we used Eqs. (7) and (9) to obtain a simpler equation for a given $T$ below $T_t$, namely,

$$H_\lambda^*-H_1=B^*(T_t-T)^{1/\phi} \ . \tag{10}$$

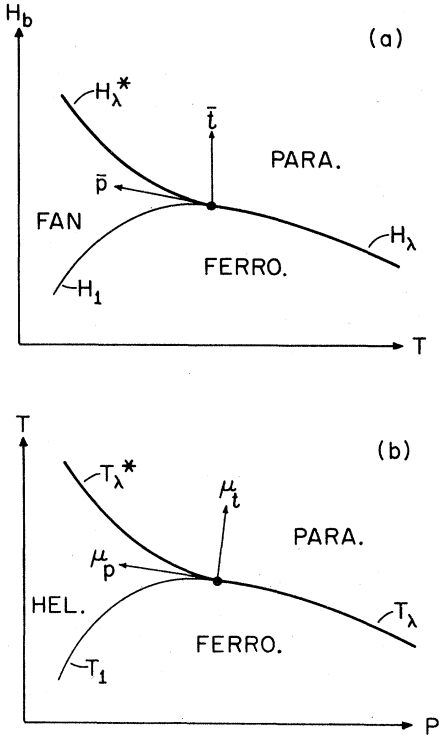


FIG. 17. (a) Scaling axes $\bar{p}$ and $\bar{t}$ at the upper triple point of MnP. (b) Scaling axes $\mu_p$ and $\mu_t$ at a LP.

Here, $B^*=B_1-B_3$ is a constant. Equation (9) contains fewer parameters than any of the Eqs. (7)–(9), and is more suitable for obtaining $\phi$.

Anticipating our later conclusion that the upper triple point is a LP, we now relate the scaling axes which are used here to those in the standard discussions of a LP. In these standard discussions, the phase diagram is in the $PT$ plane, and not in the $TH_b$ plane. The scaling hypothesis near a LP is discussed in Ref. 1, and the phase diagram in the $PT$ plane is discussed in Ref. 55, among others. As pointed out by Hornreich,[1] the scaling fields $\mu_t$ and $\mu_p$ near the LP are linear combinations of the physical variables $(T-T_L)$ and $(P-P_L)$. In Fig. 17(b) we show these scaling axes schematically. The axis $\mu_p$ in Fig. 17(b) corresponds to the axis $\bar{p}$ in Fig. 17(a). Also, the optimal choice for $\mu_t$ will correspond to the optimal choice for $\bar{t}$. Our choice for the $\bar{t}$ axis (parallel to the $H_b$ axis) will correspond to some nonoptimal choice of $\mu_t$, but will still lead to the correct asymptotic behavior.

The formal correspondence between the standard phase diagram for a LP and the phase diagram in MnP is given in Fig. 17. We now discuss the physical origin of this correspondence. In those theoretical models of the LP that involve competing exchange interactions, $P$ is a parameter which governs the rela-

tive strengths of these interactions. In MnP, the experimental evidence is that a temperature change (at constant $H$) leads to a change in the relative strengths of the competing exchange interactions.[13] Thus, in a sense, the temperature in the case of MnP plays a similar role to that played by $P$ in the theoretical discussions. This should not be taken to mean that a temperature change in MnP is identical in its effects to a pressure change in the theoretical models. However, there is a rough correspondence between the $T$ axis near the upper triple point in MnP and the $P$ axis in theoretical discussions of a LP.

The thermal axis $\tilde{t}$ for critical points on the line $H_\lambda(T)$ was discussed in Sec. IV C 3. It was pointed out that for $T \ll T_C$, the thermal axis can be chosen to be parallel to the $H_b$ axis. The direction of the thermal axis $\bar{t}$ at the upper triple point is the limiting direction of $\tilde{t}$ as $T \to T_t$.[50,53] Thus, $\bar{t}$ is taken to be parallel to the $H_b$ axis. In theoretical discussions of the LP, the thermal axis $\mu_t$ essentially corresponds to the $T$ axis. Thus, the $T$ axis in the theoretical discussions roughly corresponds to the $H_b$ axis in MnP. Physically, a large $H_b$ opposes the ordering of magnetic moments along the $c$ axis of MnP, just as a high temperature in the usual case opposes magnetic order.

It should be noted that Eqs. (7)–(10) are based on the assumption of generalized scaling only. They are not based on the formal correspondence between Figs. 17(a) and 17(b), or on the physical explanation of this correspondence.

### 2. *Least-squares fits*

Least-squares fits were performed in order to obtain $\phi$. The fits were to Eq. (10), except that we used the measured fields $H_{01}$ and $H_{0\lambda}^*$ instead of the internal fields $H_1$ and $H_\lambda^*$. The demagnetization corrections are discussed later. In all the fits we used only matched pairs $(H_{01}, H_{0\lambda}^*)$ which were measured at the same $T$. Isolated data points (for either $H_{01}$ or $H_{0\lambda}^*$) that did not have matching partners were not included. Because the data for samples 1 and 2 were usually taken in pairs, the fits included most of the experimental points for these samples. However, for sample 3 there were quite a few data points that had no matching partners.

Two types of fits to Eq. (10) were made. In the first, the parameters $B^*$, $\phi$, and $T_t$ were all allowed to vary. In the second, $T_t$ was held fixed, and only $B^*$ and $\phi$ were allowed to vary. Here, we chose $T_t = 121$ K, which was the value obtained from the data for sample 2. The effect on $\phi$ of the ±1-K uncertainty in $T_t$ was evaluated by repeating the fits with $T_t$ held fixed at 120 and 122 K.

The fits of the first type gave the following results. For sample 1 (with $H_{01}$ and $H_{0\lambda}^*$ obtained from susceptibility data), $T_t = 120.4 \pm 0.2$ K, $\phi = 0.625 \pm 0.006$, and $B^* = 0.031 \pm 0.002$. The units for $B^*$ are such that the difference $H_{0\lambda}^* - H_{01}$ is in units of kOe when $T$ is in units of degrees K. The quoted uncertainties are standard deviations. The fit for sample 1 is shown in Fig. 18. For sample 2 we made separate fits for data taken in three different experimental runs. For the run in which the MS was measured with $\hat{l} \parallel c$ we obtained $T_t = 120.7 \pm 0.2$ K, $\phi = 0.633 \pm 0.009$, and $B^* = 0.035 \pm 0.003$. For the two runs in which the MS was measured with $\hat{l} \parallel b$ we obtained $\phi = 0.74$ and 0.76, and $T_t = 117$ K (for both runs). We regard the values for the last two runs as unreliable for the following reasons: (a) The value $T_t = 117$ K is clearly lower than the true value. (b) Matched pairs $(H_{01}, H_{0\lambda}^*)$ were obtained only below 108 K in one of these runs, and below 109 K in the other. (In the run with $\hat{l} \parallel c$, matched pairs were obtained up to 119 K.) (c) There is some evidence that a small-field misalignment affected the results with $\hat{l} \parallel b$ (see Sec. IV D 5). Turning to sample 3, we made a fit to all matched pairs obtained below 20 kOe. The fit gave $T_t = 120.0 \pm 1.3$ K, and $\phi = 0.66 \pm 0.06$.

The fits with $T_t$ held fixed at 121 K led to the following results: $\phi = 0.61 \pm 0.03$ for sample 1; $\phi = 0.62 \pm 0.05$ for sample 2 with $\hat{l} \parallel c$; $\phi = 0.64 \pm 0.03$ and $0.65 \pm 0.03$ for the two runs with $\hat{l} \parallel b$ in sample 2; and $\phi = 0.62 \pm 0.04$ for sample 3. Here the quoted uncertainties include the uncertainty in $\phi$ which

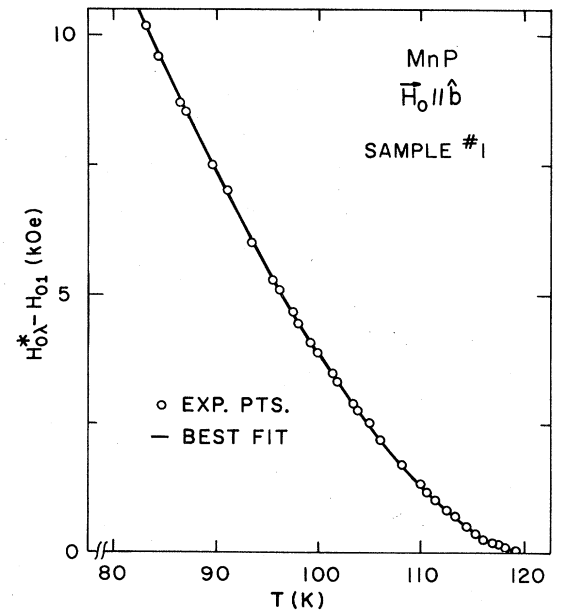


FIG. 18. Least-squares fit of the data for sample 1 to Eq. (10), with $B^*$, $T_t$, and $\phi$ treated as adjustable parameters. The ordinate is the difference between the applied magnetic fields at the para-fan and ferro-fan transitions. The parameters of the fit are given in the text.

resulted from the ±1-K uncertainty in $T_t$.

The results which were quoted above were not corrected for demagnetization effects. However, our estimates showed that the error in $\phi$ which was caused by using applied fields instead of internal fields was smaller than 0.01, in all cases.

We have also considered the question of whether Eq. (10), which describes the asymptotic behavior near the triple point, is suitable for $T$'s as low as 80 K. Suppose that Eq. (10) fails at the lower end of the range 80–121 K. One then expects that the exponent $\phi$ obtained from a fit over the entire range will differ from that obtained from a fit over a more restricted range near the triple point. For this reason, some checks were made for the dependence of $\phi$ on the minimum temperature $T_{\min}$ which was still included in the fit. The two sets of data which were examined were the set for sample 1, and the set for sample 2 with $\hat{l} \| c$. It was found that for all $T_{\min}$'s which were below 110 K, the exponent $\phi$ was the same to within several percents. Also, there was no obvious systematic dependence of $\phi$ on $T_{\min}$. Reliable values for $\phi$ could not be obtained for $T_{\min} \gtrsim 110$ K because the uncertainty in $\phi$ became large when only a few data points were included in the fit.

Based on the results of the least-squares fits, we estimate that the crossover exponent is $\phi = 0.63 \pm 0.04$.

#### 3. Discussion

The crossover exponent $\phi$ was calculated using an $\epsilon$ expansion, where $\epsilon = 4 + (m/2) - d$ for a LP. The result, to first order in $\epsilon$, is[55]

$$\phi = \tfrac{1}{2} + [(n+2)/4(n+8)]\epsilon \ . \qquad (11)$$

For $d = 3$ and $n = m = 1$, this gives $\phi = 0.625$. Our experimental value, $\phi = 0.63 \pm 0.04$, is in good agreement with this prediction. Thus, the experimental value for $\phi$ is consistent with the interpretation that the upper triple point is a LP.

## VI. PHASE DIAGRAM WITH NONZERO $H_c$

In this section we discuss the phase diagram near the upper triple point in the presence of a $c$ component of $\vec{H}$. This component is the thermodynamic field which is conjugate to the order parameter of the ferro phase, i.e., the ordering field for the ferro phase. The experimental results are interpreted on the *assumption* that the triple point is a LP. The discussion will be qualitative for two reasons: (i) The existing theory is at an early stage. It consists of calculations based on a Landau-type theory,[56] and of mean-field calculations for the Ising model.[57] (ii) Only a rough picture of the phase diagram with $H_c \neq 0$ was obtained experimentally, because large demagnetization effects complicated the interpretation of the data.

### A. Expected phase diagram near the LP

#### 1. Intrinsic phase diagram

A qualitative picture for the expected phase diagram in the $TH_bH_c$ space is obtained from Refs. 56 and 57. To translate the theoretical results in these references to the case of MnP we use the correspondence shown in Fig. 17. We also replace $H$ (the theoretical ordering field for the ferro phase) by $H_c$. Finally, we modify Fig. 1 in Ref. 56 in that we draw the line $H_1(T)$ tangent to the two segments of the $\lambda$ line in the $H_bT$ plane. This is in accordance with Refs. 52 and 57 and the experimental data. The phase diagram is sketched in Fig. 19(a). A sketch of

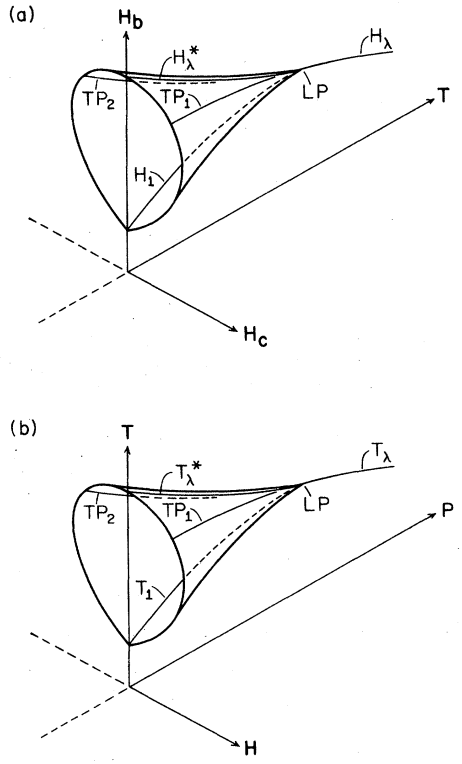


FIG. 19. Sketch of the phase diagram near a LP, in the presence of an ordering field for the ferro phase. (a) Expected phase diagram for MnP. Here, the ordering field is $H_c$. The helicoidal phase is inside the "funnel." $TP_1$ and $TP_2$ are lines of tricritical points, which separate the surface of critical points (upper part of the funnel) from the surface of first-order points (lower part of the funnel). (b) Phase diagram in the standard theoretical coordinate system. All magnetic fields in this figure are internal fields.

the phase diagram in the usual theoretical coordinate system $TPH$ is shown in Fig. 19(b). All the magnetic fields in Fig. 19 are internal magnetic fields. For this reason we call the phase diagram in Figs. 19(a) or 19(b) the intrinsic phase diagram. The measured phase diagram is different because it is influenced by demagnetization effects.

Figure 19 shows that the helicoidal (fan) phase is bounded by a surface which has the shape of a noncircular funnel whose apex is at the LP. The top part of this funnel, above the lines $TP_1$ and $TP_2$, is a surface of critical points. That part of the funnel which is below the lines $TP_1$ and $TP_2$ is a surface of first-order transition points. The lines $TP_1$ and $TP_2$ are lines of tricritical points.

In Fig. 19(a), that portion of the $TH_b$ plane which is bounded from above by the lines $H_1(T)$ and $H_\lambda(T)$ is a surface of coexistence for two ferromagnetic phases, $F^+$ and $F^-$, with opposite directions for the magnetization components $M_c$. The phase $F^+$ exists when $H_c \geq 0$, while $F^-$ exists when $H_c \leq 0$. These two ferromagnetic phases become indistinguishable on the critical line $H_\lambda(T)$ in the $TH_b$ plane. There is no corresponding transition out of the $TH_b$ plane, i.e., the line $H_\lambda(T)$ does not evolve into a surface of phase transitions when $H_c$ is added to the problem. Also, if $H_c$ is positive, say, then there is no distinction between the $F^+$ phase and the para phase, because the para phase has a field-induced positive $M_c$. Only when $H_c = 0$ can one distinguish between the para phase (with $M_c = 0$) and a ferro phase (with $M_c \neq 0$).

Phase diagrams with some similarity to that in Fig. 19 were discussed earlier in the literature in connection with other multicritical points. Examples are (1) the phase diagram near the fourth-order point ${}^4R_0$ in Fig. 2 of Ref. 53, and (2) the phase diagram near the bicritical point of an antiferromagnet in the presence of a staggered field, which is shown in Fig. 8 of Ref. 58 and in Fig. 22 of Ref. 59. In these examples, phases with different order parameters meet at a multicritical point, and one of the thermodynamic fields is the ordering field for one of the phases.

Consider Fig. 19(b). By taking a cut at a constant $P$, below $P_L$, we obtain the sketch shown in Fig. 20(a). In this figure, $TP_2$ and $TP_2$ are tricritical points, which separate the upper portion of the ferro-helicoidal boundary (line of critical points) from the lower portion (line of first-order points). Near $T_1$, the ferro-helicoidal line, for either $H > 0$ or $H < 0$, has a finite slope. This slope is related by the Clapeyron-Clausius relation to the jumps in the entropy $S$ and magnetization $M$, i.e., $(\partial T/\partial H)_P = -\Delta M/\Delta S$. A figure which is similar to Fig. 20(a) is also obtained from Fig. 19(a) by taking a cut at a constant $T$, below $T_L$. In this case, the variables $T$ and $H$ of Fig. 20(a) are replaced by $H_b$ and $H_c$, respectively. The slope $(\partial H_b/\partial H_c)_T$ of the ferro-

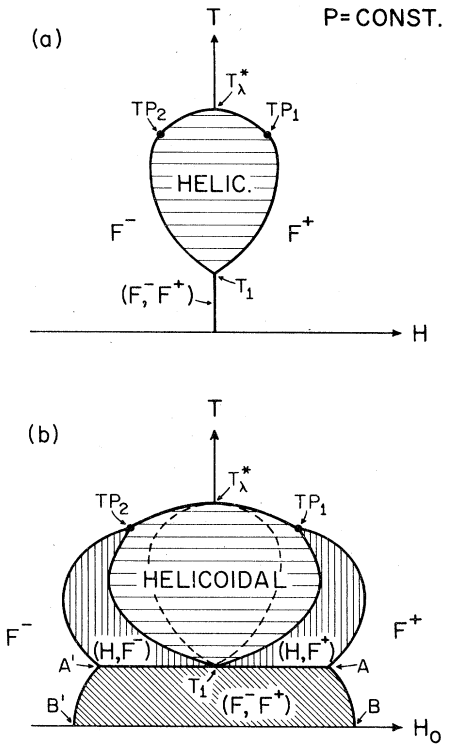


FIG. 20 (a) Phase diagram obtained from Fig. 19(b) by taking a cut at a constant $P$, below $P_L$. The points $TP_1$ and $TP_2$ are tricritical points. Transitions above these points are of second order. Transitions below the points $TP_1$ and $TP_2$ are of first order. That portion of the $T$ axis which is below $T_1$ is a line of coexistence for the two ferro phases: $F^+$ and $F^-$. The magnetic field $H$ is the internal field. (b) The phase diagram obtained from part (a) by taking demagnetization effects into account. Here, $H_0$ is the applied magnetic field. The region $(H,F^+)$ is a region of coexistence for helicoidal and $F^+$ domains. The region $(F^-,F^+)$ is a coexistence region for $F^-$ and $F^+$ domains. For comparison, the boundary of the helicoidal phase in part (a) is also shown in part (b) as a dashed curve.

helicoidal boundary, at a point on the first-order portion of this boundary, is then related to the jumps $\Delta M_c$ and $\Delta M_b$ of the $c$ and $b$ magnetization components.

### 2. *Demagnetization effects*

We start the discussion of the demagnetization effects by considering the theoretical phase diagram in Fig. 19(b), rather than its analog for MnP which is shown in Fig. 19(a). The reason for this is that only one of the axes in Fig. 19(b) is a magnetic field, whereas two of the axes in Fig. 19(a) are magnetic fields. The more complicated case of MnP will be discussed later.

Near the LP, the intrinsic susceptibility $\chi_{in}=M/H$ is large (see Sec. VII). Moreover, in the ferro phase there is a spontaneous magnetization. Under these circumstances, and for a typical demagnetizing factor ($N$ of order unity), demagnetization effects are important. To discuss these effects we first assume that the sample is ellipsoidal. This assumption is relaxed later.

Consider Fig. 20(a), and focus attention on the line of second-order transitions, i.e., the portion of the phase boundary above $TP_1$ and $TP_2$. For a given $T$, the applied field $H_0(2)$ at the transition is higher than the internal transition field $H(2)$. The two fields are related by Eq. (2).

Consider next a first-order transition from the helicoidal phase to a ferro phase ($F^+$ or $F^-$), i.e., below the points $TP_1$ and $TP_2$ in Fig. 20(a). Let the internal transition field, for a fixed $T$, be $H(1)$. As a function of $H_0$, the transition will commence at $H_0=H(1)+NM_H$, and will end at $H_0=H(1)+NM_F$, where $M_H$ and $M_F$ are the magnetizations on the helicoidal and ferro sides of the transition. Between these two values of $H_0$, the sample will be in a mixed "phase" in which domains of helicoidal and ferro phases coexist. The ferromagnetic domains are of the type $F^+$ for $H_0>0$ and $F^-$ for $H_0<0$. The coexistence regions for helicoidal and ferromagnetic domains will be labeled as $(H,F^+)$ and $(H,F^-)$. The width of each of these regions is

$$\Delta H_0=N(M_F-M_H)=N\Delta M \quad . \tag{12}$$

This width approaches zero as the tricritical points $TP_1$ and $TP_2$ are approached. At $T=T_1$, we have $H(1)=0$ and $M_H=0$. Then the region $(H,F^+)$ extends from $H_0=0$ to $H_0=NM_s(T_1)$, where $M_s(T_1)$ is the spontaneous magnetization of an $F^+$ domain at $T_1$. A similar result holds for the $(H,F^-)$ region.

In Fig. 20(a), that portion of the $T$ axis which is below $T_1$ is a line of coexistence for the $F^+$ and $F^-$ phases. When a positive $H_0$ is applied at $T<T_1$, the $F^+$ domains grow at the expense of the $F^-$ domains until, at $H_0=NM_s(T)$, the entire sample is occupied by the $F^+$ phase. For a negative $H_0$, the roles of $F^+$ and $F^-$ are interchanged. Thus, in the $TH_0$ plane, the region $(F^-,F^+)$, where the two ferro phases coexist, is an area instead of a line.

These considerations lead to the phase diagram in Fig. 20(b). There are five types of boundaries in this figure: (1) the helicoidal-ferro boundary of second-order phase transitions, on the upper arch between $TP_1$ and $TP_2$; (2) the helicoidal-to-$(H,F^+)$ and helicoidal-to-$(H,F^-)$ boundaries, along the line from $TP_1$ to $T_1$ to $TP_2$; (3) the $(H,F^+)-F^+$ and $(H,F^-)-F^-$ boundaries, along the lines $TP_1-A$ and $TP_2-A'$; (4) the $(F^-,F^+)-(H,F^+)$ and $(F^-,F^+)-(H,F^-)$ boundaries, along the horizontal line $AA'$; (5) the $(F^-,F^+)-F^+$ and $(F^-,F^+)-F^-$ boundaries, along the lines $AB$ and $A'B'$. A sharp first-order transition from $(F^-,F^+)$ to a pure helicoidal phase occurs only at the point $T_1$.

A comment concerning terminology should be made. When $H$ is zero, the transition at $T_1$ is called the ferro-helicoidal transition, while the transition at $T_\lambda^*$ is called the para-helicoidal transition. When $H$ is nonzero, there is no distinction between the para phase and a ferro phase. We then refer to the transitions on the arch from $TP_1$ to $TP_2$, in Fig. 20(a) or 20(b), as second-order ferro-helicoidal transitions. The transition at $T_1$ is the first-order ferro-helicoidal transition.

Figure 20(b) was constructed on the assumption that the sample was ellipsoidal. If the sample is not ellipsoidal, $H$ is not uniform inside the sample. Then, the boundaries separating the various regions in Fig. 20(b) are broadened along the direction of the $H_0$ axis. The horizontal boundary $AA'$ is unique in that it remains sharp, although its termination points $A$ and $A'$ will be poorly defined experimentally. The zero-field transitions at $T_1$ and $T_\lambda^*$ are, of course, unaffected by the sample's shape, and they remain sharp.

Turning to MnP, two of the thermodynamic fields are the $b$ and $c$ components of $\vec{H}$. One then has to consider demagnetization effects associated with the $b$ and $c$ directions separately. For the sample which we used (No. 3, with $N_b\cong N_c$), demagnetization effects for the $c$ direction had a much greater influence on the measured phase diagram than those for the $b$ direction. The reason for this was that near the LP the susceptibility associated with the $c$ direction was much larger than that for the $b$ direction.

As a first approximation, we ignore the demagnetization effects for the $b$ direction, and set $H_b$ equal to the $b$ component of the applied field, $H_{0b}$. The analog of Fig. 20(b) is then constructed by replacing $P=$const by $T=$const, $T$ by $H_b$ (which is set equal to $H_{0b}$), and $H_0$ by $H_{0c}$. The result is shown in Fig. 21.

If the small demagnetization effects for the $b$ direction are included, the phase diagram in the $H_{0b}-H_{0c}$ plane will still be quite similar to that in Fig. 21. The main changes are (1) slight shifts in the values of $H_{0b}$ at points such as $H_{01}$, $H_{0\lambda}^*$, $TP_1$, $TP_2$, $A$, and $A'$, and (2) a slight broadening of the measured "transitions" on the horizontal line from $A$ to $A'$.

In Sec. IV D 5 the error in $H_{0\lambda}^*$ which was caused by a misalignment of $\vec{H}_0$ was discussed. We return to this problem briefly. Figure 21 indicates that the area occupied by the helicoidal phase in the $H_{0b}H_{0c}$ plane of applied magnetic fields is larger than that in the $H_bH_c$ plane of internal fields. This "expansion" of the helicoidal phase increases with increasing $N_c$. Also, in the $H_{0b}H_{0c}$ plane the curvature of the phase boundary at $H_{0\lambda}^*$ decreases with increasing $N_c$. This means that for a given angular misalignment of $\vec{H}_0$, in the $bc$ crystallographic plane, the misalignment error in $H_{0\lambda}^*$ will decrease with increasing $N_c$.

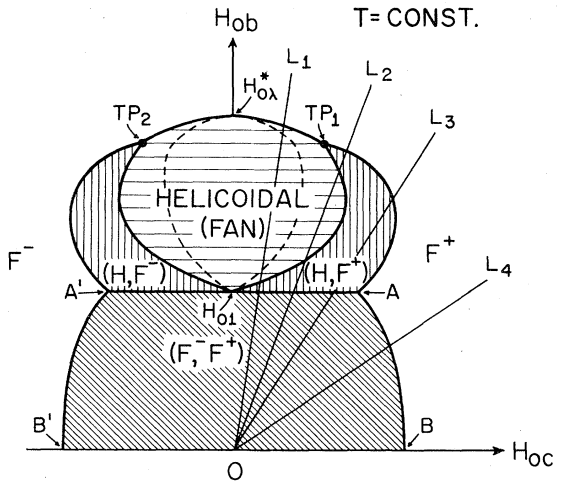


FIG. 21. Analog of Fig. 20(b) for the case of MnP. Here, $H_{0b}$ and $H_{0c}$ are the $b$ and $c$ components of the applied field $\vec{H}_0$, respectively. Demagnetization effects associated with the $b$ direction are not included in this figure. Each of the lines $L_1, \ldots, L_4$ indicates a path which is followed in a measurement at a constant angular setting of $\vec{H}_0$.

### B. Experimental results

Magnetostriction measurements were made on sample 3. The data were taken in an electromagnet which could be rotated. The field $\vec{H}_0$ was always in the $bc$ plane, but its direction in that plane was adjustable. From the patterns of the MS as a function of field direction, the angular setting of the electromagnet which corresponded to $\vec{H}_0 \| b$ was determined to within 0.1°. The angle $\theta$ between $\vec{H}_0$ and the $b$ axis was then known to within 0.2°. MS data were taken in the configurations $\hat{l} \| b$ and $\hat{l} \| c$. Traces of the MS were obtained at fixed temperatures and at fixed angular settings for $\vec{H}_0$.

The anomalies of the MS at the transition fields $H_{01}(T)$, $H_{0\lambda}(T)$, and $H^*_{0\lambda}(T)$, for $\vec{H}_0 \| b$, were described in Sec. IV. The dependence of the MS near each of these transition fields on the angle $\theta$ will now be described.

#### 1. *Behavior near* $H_{0\lambda}$

With $\vec{H}_0$ parallel to the $b$ axis, and for $T_t < T < T_C$, the MS curve had an inflection point at the para-ferro transition field $H_{0\lambda}$. As $\theta$ increased from zero, the transition became progressively less pronounced, and it disappeared entirely above a certain value of $\theta$. For temperatures that were only a few degrees K above $T_t = 121$ K, the transition was observed only when $\theta$ was smaller than $\sim 1°$. This is illustrated by the results in Fig. 22(a). In another set of runs near 285 K, the same general pattern was observed, but a very broad inflection in the MS curve was still observed at $\theta = 10°$. This is shown in Fig. 22(b). Note that the apparent transition field in Fig. 22(b) decreases as $\theta$ increases.

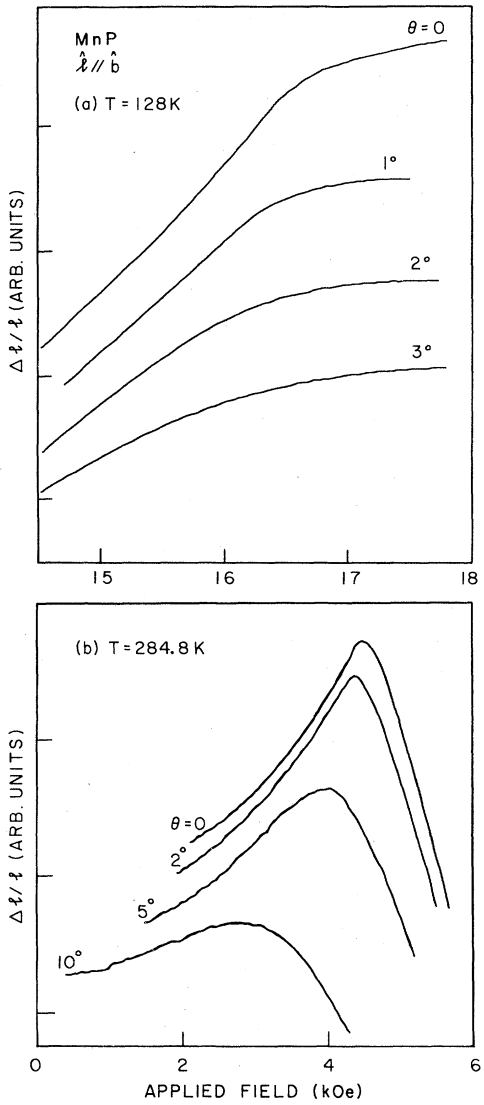


FIG. 22. (a) Dependence of the magnetostriction $\Delta l$ at 128 K on the angle $\theta$ between $\vec{H}_0$ and the $b$ axis. The applied field $\vec{H}_0$ is in the $bc$ plane. (b) Dependence of the MS at 284.8 K on the angle $\theta$. These data are for sample 3. In both (a) and (b) the zero for the ordinate scale is different for different curves.

#### 2. *Behavior near* $H_{01}$

For $\theta = 0$, and when $T_\alpha < T < T_t$, the ferro-fan transition at $H_{01}$ was accompanied by a fairly abrupt change in $l$. For nonzero $\theta$, the magnitude of the change in $l$ decreased with increasing $|\theta|$. The value

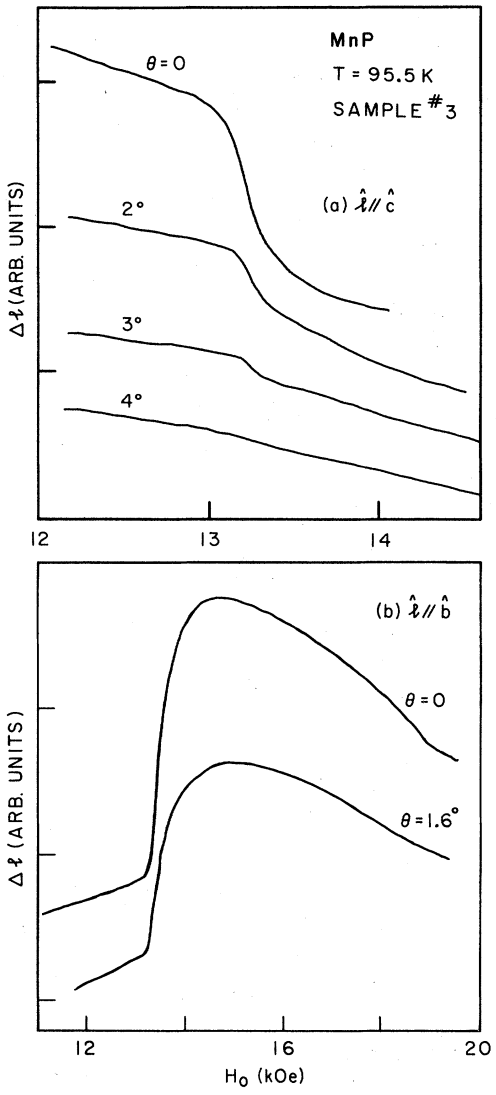


FIG. 23. Dependence of the MS at 95.5 K on the angle $\theta$. (a) Results for the configuration $\hat{l} \parallel c$. (b) Results for the configuration $\hat{l} \parallel b$. In both (a) and (b) the zero of the ordinate scale is different for different curves.

of $H_0$ where the change in $l$ occurred was nearly independent of $\theta$. This is illustrated by the data in Fig. 23(a), and also by the behavior near the lower transition in Fig. 23(b).

For a fixed $T$, there was a maximum angle $\theta_m$ at which an abrupt change in $l$ was still detectable. At $\theta_m$, the change in $l$ was often 2–3 orders of magnitude smaller than the change at $\theta = 0$. The value of $\theta_m$, for a given $T$, depended somewhat on the resolution of the dilatometer during the particular experimental run, and it was also somewhat larger for the configuration $\hat{l} \parallel b$ than for $\hat{l} \parallel c$. The latter observation might be related to the fact that the magnitude of the change in $l$ was larger for $\hat{l} \parallel b$. For a given instrumental resolution, $\theta_m$ decreased with increasing $T$. Typical values of $\theta_m$ were 10° at 77 K, and 1° at 115 K.

### 3. Behavior near $H_{0\lambda}^*$

When $\vec{H}_0 \parallel b$, and for $T < T_t$, the MS curve had an inflection point at the para-fan transition field $H_{0\lambda}^*$. As $\theta$ increased from zero, the transition became broader and less pronounced. The apparent transition field, at the inflection point, decreased with increasing $\theta$. This is illustrated by the higher-field portion of Fig. 23(b). For a given $T$, an inflection point in the MS curve was observed only for $\theta < \theta_m^*$. The value of $\theta_m^*$ decreased with increasing $T$. Approximate values of $\theta_m^*$ at typical temperatures were 2.5° at 95.5 K, 1° at 111 K, and 0.5° at 116 K.

### 4. Boundaries in the $H_{0b}H_{0c}$ plane

Figure 24 shows the locations of the apparent phase transitions for three representative temperatures. The axes in this figure are components of the applied (external) magnetic field. Note that the scales for the two axes are different, and that all the data points are in a region where $H_{0c} \ll H_{0b}$.

For each temperature, the data points in Fig. 24 lie on two disconnected branches: (1) the lower horizontal branch, which is the locus of the abrupt jumps in the MS curves, for various $\theta$'s, and (2) the "arch," which is the locus of the inflection points of the MS curves for various $\theta$'s.

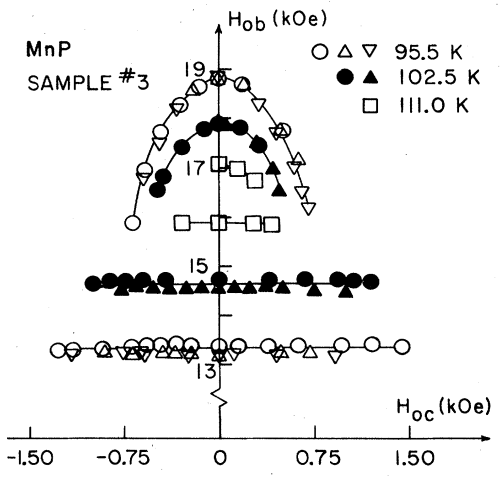


FIG. 24. Observed phase diagrams in the $H_{0c}H_{0b}$ plane, at three temperatures. The coordinate axes are the $b$ and $c$ components of the applied field $\vec{H}_0$. For each temperature, data points on the horizontal line correspond to discontinuities in the MS curves for different $\theta$'s, while data points on the "arch" correspond to inflection points in the MS curves.

### C. Discussion

#### 1. Results above $T_t$

The theory for the phase diagram near the line $H_{0\lambda}(T)$ indicates that the second-order transition on this line disappears for $\theta \neq 0$. In spite of this, MS data taken at a *small* $\theta$ should still show an anomaly (but not a singularity) in the derivative $\partial l/\partial H_0$. The anomaly should become smaller with increasing $\theta$. The experimental results are in general agreement with the expected behavior.

#### 2. Magnetostriction below $T_t$

The interpretation of the data for $T < T_t$ is based on the phase diagram in Fig. 21, in which demagnetization effects are included.

Consider the "transition" from $(F^-,F^+)$ to $(H,F^+)$, at a point between $H_{01}$ and $A$ in Fig. 21. At this transition: (1) some regions of the sample change from ferro to helicoidal, and (2) some other regions change from $F^-$ to $F^+$. Because the helicoidal and ferro phases have different properties, a discontinuity in the sample's length $l$ is expected. The change of some regions of the sample from $F^-$ to $F^+$ should not affect $l$ because the MS of a ferro region (measured with $\hat{l}$ parallel to a symmetry axis) is an even function of the direction cosines of the magnetization.[60] Thus, the magnitude of the change in $l$ is a measure of the fraction of the sample's volume which undergoes a ferro-helicoidal transition. Near the $H_{0b}$ axis, the $(H,F^+)$ "phase" consists mainly of helicoidal domains, whereas near the point $A$ it consists mainly of $F^+$ domains. Therefore, the discontinuity in $l$ is expected to decrease with increasing $\theta$. Similar considerations apply to the "transition" on the line between $H_{01}$ and $A'$. Also, from Fig. 21 the $b$ component of $\vec{H}_0$ is expected to be constant on the boundary $AA'$. The experimental data in Figs. 23 and 24 are in agreement with these predictions.

For an ellipsoidal sample, the magnitude of $H_{0c}$ at the point $A$ (or $A'$) is $H_{0c}(A) = N_c M_c(F)$, where $M_c(F)$ is the $c$ component of the magnetization of a ferro domain at $H_{01}$. For our sample (No. 3), we estimate that the average value of $N_c$ was approximately 2.3. To estimate $M_c(F)$ we assumed that the magnitude of the magnetization $\vec{M}$ of a ferro domain was nearly constant for $77 < T < 121$ K (which is well below $T_C$). The magnitude of $\vec{M}$ was taken to be equal to the saturation magnetization at 77 K. Then, using the data for $M_b$ as a function of $H_b$,[15] the magnitude of $M_c(F)$ was estimated. This led to an estimate for $H_{0c}(A)$. Because the point $A$ depends on temperature (Fig. 21 is for a particular temperature), the estimate for $H_{0c}(A)$ was temperature dependent.

Transitions which correspond to points on the line $AA'$ were observed only for $\theta < \theta_m$. If the sample were ellipsoidal, the $c$ component of the applied transition field at $\theta_m$ should have been equal to $H_{0c}(A)$. However, our data show that $H_{0c}$ for the transition at $\theta_m$ was larger than the estimated average for $H_{0c}(A)$, by a factor of 1.6, typically. We attribute this difference to the nonellipsoidal shape of the sample, which caused the internal field $H_c$ in some regions to be smaller than the average over the entire sample. For these regions, the value of $H_{0c}(A)$ should have been higher than the average. The high sensitivity of the dilatometers allowed the transition in these regions to be detected, even when these regions occupied only a small fraction of the sample's volume.

Consider Fig. 21. Measurements for fixed $\theta$'s correspond to measurements along lines such as $L_1, \ldots, L_4$. Moving along $L_1$, a second-order transition should be observed when the helicoidal-ferro boundary (between the points $H^*_{0\lambda}$ and $TP_1$) is crossed. This transition should appear as an inflection point in the MS curve, corresponding to a $\lambda$ anomaly in $\partial l/\partial H_0$. The value of $H_{0b}$ at this transition should decrease with increasing $|\theta|$. The experimental data for small $\theta$ agree with these predictions. The upper portion of each of the "arches" in Fig. 24 is interpreted as a line of second-order helicoidal-ferro transitions.

The location of the tricritical points $TP_1$ and $TP_2$ was calculated in Refs. 56 and 57. The theoretical results suggest that the lowest portions of each of the arches in Fig. 24 are below the tricritical points. That is, the lowest data points on each arch probably correspond to transitions on lines such as $L_2$ or $L_3$ in Fig. 21 rather than to helicoidal-ferro second-order transitions on lines such as $L_1$.

We, therefore, consider the line $L_2$ which passes through the upper corner of the $(H,F^+)$ region. On each of the two boundaries of this region one expects a change in the slope of the MS curve. However, the observation of two distinct changes in slope might be difficult because: (1) the points where the line $L_2$ enters and leaves the $(H,F^+)$ region are close to each other, and (2) in a nonellipsoidal sample the change in slope is not sharp. Thus, what might be observed in practice is a single broad transition. In other words, when the region $(H,F^+)$ which separates the helicoidal phase from the $F^+$ phase is narrow, one may observe a single broad transition from the helicoidal phase to the $F^+$ phase. We believe that the low portions of each of the arches in Fig. 24 correspond to just such broad transitions. However, we cannot rule out the possibility that mean-field theory gives a poor estimate for the location of the tricritical points, and that the low portions of the arches are still on the second-order boundary from a $TP_1$ to $TP_2$. Nor can we rule out the possibility that some of the observed broad transitions correspond to $(H,F^+) - F^+$ transitions on lines such as $L_3$.

Consider the line $L_1$, again. In principle, a change

in the slope of the MS curve is expected when the boundary between the $(H,F^+)$ region and the helicoidal phase is crossed. Experimentally, this "transition" was not observed. The presumed reasons for this are: (1) the transition in the nonellipsoidal sample was broad, and (2) the change in slope was masked by the relatively large abrupt change in $I$ at the nearby transition from $(F^-,F^+)$ to $(H,F^+)$.

Finally, consider the line $L_4$. In principle, the "transition" from $(F^-,F^+)$ to $F^+$, on the line $AB$, should be associated with a change in the slope of the MS curve. Experimentally, such a change in slope was observed in only one experimental run. For this run, $\theta$ was 90° (i.e., $\vec{H}_0 \| c$), and $T$ was 77 K. The observed transition (at the point $B$) was broad, presumably because the sample was not an ellipsoid.

#### 3. Phase boundaries below $T_t$

To summarize, the phase boundaries in Fig. 24 are interpreted as follows. For a given $T$, the horizontal line of data points corresponds to the line $AA'$ in Fig. 21. The upper part of any arch in Fig. 24 corresponds to the line of second-order helicoidal-ferro transitions, between the points $TP_1$ and $TP_2$ in Fig. 21. The lower part of any arch probably (but not definitely) corresponds to broad transitions on lines such as $L_2$ in Fig. 21. The locations of the tricritical points on each of the arches cannot be determined from the data.

## VII. TRANSVERSE DIFFERENTIAL SUSCEPTIBILITY

### A. Expected behavior near a LP

In this section it is assumed that the dc field $\vec{H}_0$ is parallel to the $b$ axis. The disorder-to-order transitions on the boundaries $H_{0\lambda}(T)$ and $H^*_{0\lambda}(T)$ are associated with the development of a long-range order of the $c$ component of the local magnetization. This long-range order is uniform ($q=0$) for the ferro phase, and oscillatory ($q \neq 0$) for the fan phase. We consider the expected behavior for the measured transverse differential susceptibility $\chi^{\perp}_m = \partial M_c/\partial h_0$, where the applied modulation field $\vec{h}_0$ is parallel to the $c$ axis, and is, therefore, perpendicular to $\vec{H}_0$.

#### 1. Para-ferro transition

The transition on the para-ferro boundary is associated with a divergence in the intrinsic susceptibility $\chi^{\perp}_{in} = \partial M_c/\partial H_c$. Because of the demagnetization effects, the measured susceptibility on this boundary is $\chi^{\perp}_m = 1/N_c$.

To describe the behavior of $\chi^{\perp}_m$ in the ferro phase, it is useful to draw an analogy to the case of an ordinary ferromagnet. For such a ferromagnet, the differential susceptibility $\chi_m$ (measured in the ferro phase at $H_0=0$) depends on the response of the ferromagnetic domains to an aligning field.[61] When the domains are readily aligned, $\chi_m$ is equal to $1/N$. This is the usual observed behavior when the modulation field $h_0$ is not too small and when the modulation frequency is not too high. We expect a similar behavior in MnP. In this case, $\chi^{\perp}_m$ plays the role of $\chi_m$. Thus, we expect that in the ferro phase of MnP, $\chi^{\perp}_m = 1/N_c$.

Therefore, the following behavior of $\chi^{\perp}_m$ as a function of $H_0$ is expected, for $T_t < T < T_C$. As $H_0$ decreases from a high value, $\chi^{\perp}_m$ increases, until it reaches the value $1/N_c$ at $H_0 = H_{0\lambda}(T)$. For $H_0 < H_{0\lambda}$, the susceptibility $\chi^{\perp}_m$ remains equal to $1/N_c$.

#### 2. Para-fan transition

The fan phase is a phase with a finite $\vec{q}$. Therefore, the uniform intrinsic susceptibility $\chi^{\perp}_{in}$ does not diverge at the para-fan boundary $H^*_\lambda(T)$. The susceptibility which diverges at $H^*_\lambda$ is the $q$-dependent susceptibility $\chi^{\perp}_{in}(\vec{q})$ for $\vec{q} = \vec{q}^*_\lambda(T)$, where $\vec{q}^*_\lambda(T)$ is the wave vector of the fan phase at $H^*_\lambda(T)$. Assuming that the triple point is a LP, $q^*_\lambda \to 0$ as the triple point is approached. Then, $\chi^{\perp}_{in}(\vec{q}^*_\lambda) \to \chi^{\perp}_{in}(0) \equiv \chi^{\perp}_{in}$ when $T \to T_t$. Therefore, moving along the boundary $H^*_\lambda(T)$, the susceptibility $\chi^{\perp}_{in}$ should diverge when $T \to T_t$. To zeroth order in $\epsilon$, this divergence is characterized by the power law $\chi^{\perp}_{in} \propto (T_t - T)^{-2}$ (Refs. 52, 55, and 62). For a fixed $T$, the susceptibility $\chi^{\perp}_{in}$ as a function of $H$ should have a peak at $H = H^*_\lambda$.[52,62]

The measured susceptibility $\chi^{\perp}_m$ is related to $\chi^{\perp}_{in}$ by the analogs of Eqs. (3) and (4). For a fixed $T$ we expect that $\chi^{\perp}_m$ vs $H_0$ will exhibit a finite peak at $H^*_{0\lambda}(T)$. Let the value of $\chi^{\perp}_m$ at $H^*_{0\lambda}(T)$ be $\chi^*_\lambda(T)$. Then, $\chi^*_\lambda$ should increase with increasing $T$, and should become equal to $1/N_c$ when $T$ reaches $T_t$.

#### 3. Ferro-fan transition

In the fan phase, $\chi^{\perp}_{in}$ is finite, so that $\chi^{\perp}_m$ is smaller than $1/N_c$. In the ferro phase, $\chi^{\perp}_m$ is expected to be equal to $1/N_c$. Thus, the transition from the fan phase to the ferro phase (which occurs when $H_0$ decreases) should be accompanied by an increase in $\chi^{\perp}_m$.

#### 4. Additional remarks

In the foregoing discussion, the expected features of $\chi^{\perp}_{in}$ and $\chi^{\perp}_m$ were obtained by assuming that the triple point was a LP. However, it turns out that qualitatively similar behaviors of $\chi^{\perp}_{in}$ and $\chi^{\perp}_m$ may also be observed near a triple point which is not a LP.

Selke considered a para-ferro-helicoidal triple point at which $q^*_\lambda$ exhibits a jump from a finite value to

zero.[63,64] The $q$-dependent susceptibility near such a triple point (which is not a LP) is sketched in Fig. 1 of Ref. 63. The qualitative behavior of the uniform ($q=0$) susceptibility is similar to that near a LP. However, we expect that the quantitative behavior (critical exponents) will be different.

It follows that the *qualitative* features of $\chi_m^\perp$ provide only a consistency check that must be satisfied if the triple point is a LP; they do not prove that it is a LP. Other data are necessary to rule out the possibility that $q_\lambda^*$ has a jump at the triple point. For MnP, recent neutron Bragg scattering experiments provide strong evidence that $q_\lambda^*$ goes continuously to zero as $T \rightarrow T_t$.[12]

### B. Experimental results and discussion

Measurements of $\chi_m^\perp$ were performed on sample 3, with $\vec{H}_0 \| b$. Data were taken at several fixed temperatures between 88 and 146 K. Some of the results for $\chi_m^\perp$ vs $H_0$ are shown in Fig. 25. The data for 125 K are typical for $T > T_t$. They show that the susceptibility increases as $H_0$ decreases toward $H_{0\lambda} = 16$ kOe. For $H_0 < H_{0\lambda}$, the susceptibility $\chi_m^\perp$ is nearly constant. These qualitative features are similar to those expected for $T > T_t$. The only deviation is the small variation of $\chi_m^\perp$ in fields below $H_{0\lambda}$. Measurements with $\vec{H}_0$ purposely misaligned relative to the $b$ axis showed that the variation of $\chi_m^\perp$ below $H_{0\lambda}$ increased rapidly with increasing misalignment. The departure from ideal of the data for 125 K is, therefore, attributed to a small unintentional misalignment of $\vec{H}_0$.

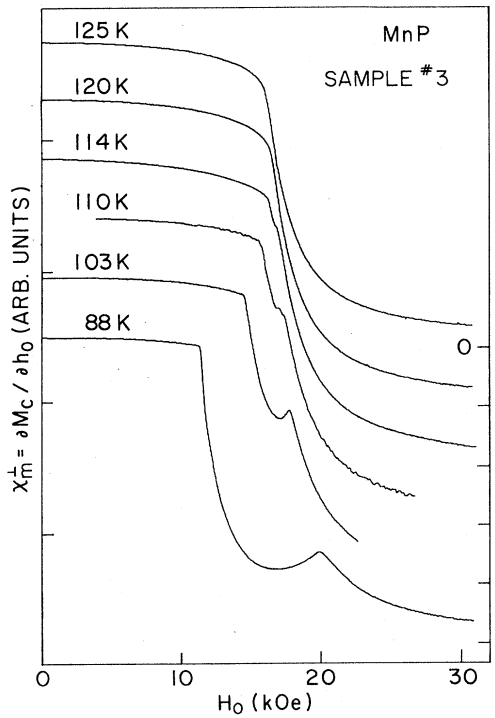


FIG. 25. Transverse differential susceptibility, $\chi_m^\perp$, measured with a steady magnetic field $\vec{H}_0$ along $b$ and a modulation field $\vec{h}_0$ parallel to $c$. Each curves shows $\chi_m^\perp = \partial M_c / \partial h_c$ (where $M_c$ is the net magnetization along $c$) as a function of $H_0$, at a fixed $T$. The curves were displaced in the vertical direction relative to each other. The zeros for successive curves are indicated by short horizontal lines on the right. Apart from this zero shift, the vertical scale is the same for all curves. The values of $\chi_m^\perp$ at $H_0 = 0$ are very nearly equal.

The behavior of $\chi_m^\perp$ for $T$ well below $T_t$ is exemplified by the data for 88 K. At this temperature, $\chi_m^\perp$ has a peak at $H_{0\lambda}^* \cong 20$ kOe. At this peak, $\chi_m^\perp$ is much lower than in the ferro phase (i.e., lower than $1/N_c$). The fan-to-ferro transition, at $H_{01} = 11.6$ kOe, is accompanied by an increase in $\chi_m^\perp$. These qualitative features are in agreement with the expected behavior.

Comparison of the trace at 103 K with that at 88 K indicates that the susceptibility peak at $H_{0\lambda}^*$ is higher for the higher temperature. This is expected because $\chi_\lambda^*$ should increase with $T$. At 110 and 114 K, the susceptibility exhibits a "shoulder" at $H_{0\lambda}^*$. That is, the peak at $H_{0\lambda}^*$ is not fully resolved. This is explained by the small separation between $H_{0\lambda}^*$ and $H_{01}$ at these temperatures. Above 116 K, no distinct feature is observed at $H_{0\lambda}^*$. This is attributed to the still smaller separation between $H_{01}$ and $H_{0\lambda}^*$.

Data for $\chi_\lambda^*$ were obtained only below 116 K. In this temperature range, $\chi_\lambda^*$ increased with increasing $T$. It is useful to compare $\chi_\lambda^*$ with the value of $\chi_m^\perp$ just below $H_{01}$. The latter value, which we call $\chi_1$, represents the susceptibility of the ferro phase at $H_{01}$. Below 116 K, the difference $\chi_\lambda^* - \chi_1$ decreased with increasing $T$. Extrapolation to temperatures above 116 K strongly suggests that $\chi_\lambda^*$ is equal to $\chi_1$ at $T_t$. Because $\chi_m^\perp$ is limited by demagnetization effects, a value of $\chi_\lambda^*$ which is as high as $\chi_1$ corresponds to a very high $\chi_{in}^\perp$. Thus, the data strongly suggest that on the para-fan boundary, $\chi_{in}^\perp$ becomes very large when $T \rightarrow T_t$.

In conclusion, all the qualitative features of the data for $\chi_m^\perp$ agree with those expected near a LP.

## VIII. EVIDENCE FOR A LIFSHITZ POINT

In this section we summarize the evidence that the upper triple point of MnP is a LP.

(i) The upper triple point is a point where paramagnetic, ferromagnetic, and helicoidal (fan) phases meet.

(ii) All available data indicate that the para-ferro and para-fan transitions are of second order.

(iii) The phase boundaries in the $TH_b$ plane have the qualitative features expected near a LP. That is,

at the triple point, the phase boundaries are tangent to each other and the λ line has an inflection point.

(iv) A quantitative analysis of $(H_\lambda^* - H_1)$ as a function of $T$ leads to a crossover exponent $\phi$ which is in agreement with the predicted value for a LP.

(v) The data for the transverse differential susceptibility $\chi_m^\perp$ are consistent with a LP.

(vi) The wave vector $\vec{q}$ in the fan phase, determined from Bragg scattering of neutrons, appears to go continuously to zero as the triple point is approached.[12] The smallest measured $q$ corresponds to a period of 32 lattice spacings. (Smaller $q$'s could not be observed because of experimental limitations.) The exponent $\beta_k$ obtained from the $T$ dependence of $q_\lambda^*$ is in rough agreement with theory.

(vii) Dispersion curves for spin waves in the ferro and screw phases (measured at $H=0$) strongly suggest a competition between ferromagnetic and antiferromagnetic interactions.[13] The quoted ratio $J_2/J_1$ for the competing exchange constants is close to that calculated for a LP. Moreover, $J_2/J_1$ is slightly $T$ dependent. Thus, at some temperature the ratio $J_2/J_1$ is expected to coincide with that for a LP.

Based on this evidence we believe that the upper triple point of MnP is a LP.

## ACKNOWLEDGMENTS

The National Magnet Laboratory is supported by the U.S. NSF. The Institute of Physics at the University of São Paulo is supported by Financiadora de Estudos e Projetos (FINEP). This work was supported in part by a joint grant from the Brazilian Conselho Nacional de Desenvolvimento Científico e Tecnológico (CNPq) and the U.S. National Science Foundation. Additional support was obtained from Fundação de Amparo à Pesquisa do Estado de São Paulo (FAPESP).

[1]R. M. Hornreich, J. Magn. Magn. Mater. 15–18, 387 (1980), and references therein.
[2]J. S. Smart, *Effective Field Theories of Magnetism* (Saunders, Philadelphia, 1966), Chap. 11, and references therein.
[3]R. M. Hornreich, M. Luban, and S. Shtrikman, Phys. Rev. Lett. 35, 1678 (1975).
[4]J. F. Nicoll, G. F. Tuthill, T. S. Chang, and H. E. Stanley, Phys. Lett. 58A, 1 (1976); and Physica (Utrecht) B 86–88, 618 (1977).
[5]S. Redner and H. E. Stanley, Phys. Rev. B 16, 4901 (1977); and J. Phys. C 10, 4765 (1977).
[6]W. Selke, Z. Phys. B 29, 133 (1978).
[7]M. E. Fisher and W. Selke, Phys. Rev. Lett. 44, 1502 (1980).
[8]R. M. Hornreich, Phys. Rev. B 19, 5914 (1979).
[9]J. Y. Buzaré, J. C. Fayet, W. Berlinger, and K. A. Müller, Phys. Rev. Lett. 42, 465 (1979); A. Aharony and A. D. Bruce, *ibid.* 42, 462 (1979).
[10]S. K. Sinha, G. H. Lander, S. M. Shapiro, and O. Vogt, Phys. Rev. Lett. 45, 1028 (1980).
[11]C. C. Becerra, Y. Shapira, N. F. Oliveira, Jr., and T. S. Chang, Phys. Rev. Lett. 44, 1692 (1980).
[12]R. M. Moon, J. W. Cable, and Y. Shapira, J. Appl. Phys. 52, 2025 (1981).
[13]K. Tajima, Y. Ishikawa, and H. Obara, J. Magn. Magn. Mater. 15–18, 373 (1980).
[14]E. E. Huber, Jr., and D. H. Ridgley, Phys. Rev. 135, A1033 (1964).
[15]T. Komatsubara, T. Suzuki, and E. Hirahara, J. Phys. Soc. Jpn. 28, 317 (1970).
[16]H. Terui, T. Komatsubara, and E. Hirahara, J. Phys. Soc. Jpn. 38, 383 (1975).
[17]C. C. Becerra, A. Paduan Filho, and N. F. Oliveira, Jr., Phys. Status Solidi (a) 33, 573 (1976).
[18]T. Komatsubara, K. Kinoshita, and E. Hirahara, J. Phys. Soc. Jpn. 20, 2036 (1965).
[19]N. Iwata, J. Sci. Hiroshima Univ. Ser. A-2 33, 1 (1969).
[20]T. Okamoto, T. Kamigaichi, N. Iwata, and E. Tatsumoto, J. Phys. Soc. Jpn. 25, 1730 (1968).
[21]B. Golding and C. A. Helms, in *Magnetism and Magnetic Materials-1974 (San Francisco)*, edited by C. D. Graham, G. H. Lander, and J. J. Rhyne, AIP Conf. Proc. No. 24 (AIP, New York, 1975), p. 292.
[22]A. Ishizaki, T. Komatsubara, and E. Hirahara, Prog. Theor. Phys. Suppl. 46, 256 (1970).
[23]T. Komatsubara, A. Ishizaki, S. Kusaka, and E. Hirahara, Solid State Commun. 14, 741 (1974).
[24]B. Golding, Phys. Rev. Lett. 34, 1102 (1975).
[25]T. Suzuki, J. Phys. Soc. Jpn. 25, 646 (1968).
[26]A. Takase and T. Kasuya, J. Phys. Soc. Jpn. 48, 430 (1980).
[27]T. Suzuki, J. Phys. Soc. Jpn. 25, 1548 (1968).
[28]A. Takase and T. Kasuya, J. Phys. Soc. Jpn. 49, 484, 489 (1980).
[29]G. P. Felcher, J. Appl. Phys. 37, 1056 (1966).
[30]J. B. Forsyth, S. J. Pickart, and P. J. Brown, Proc. Phys. Soc. London 88, 333 (1966).
[31]Y. Ishikawa, T. Komatsubara, and E. Hirahara, Phys. Rev. Lett. 23, 532 (1969).
[32]G. P. Felcher, G. H. Lander, and T. O. Brun, J. Phys. (Paris) 32, C1-577 (1971).
[33]H. Obara, Y. Endoh, Y. Ishikawa, and T. Komatsubara, J. Phys. Soc. Jpn. 49, 928 (1980).
[34]A. Takase and T. Kasuya, J. Phys. Soc. Jpn. 47, 491 (1979).
[35]T. Kamigaichi, T. Okamoto, N. Iwata, and E. Tatsumoto, J. Phys. Soc. Jpn. 24, 649 (1968).
[36]Y. Matsumura, E. Marita, and E. Hirahara, J. Phys. Soc. Jpn. 38, 1264 (1975).
[37]M. Ohbayashi, T. Komatsubara, and E. Hirahara, J. Phys. Soc. Jpn. 40, 1088 (1976).
[38]E. Maxwell, Rev. Sci. Instrum. 36, 553 (1965).
[39]N. F. Oliveira, Cryogenics 15, 293 (1975).
[40]N. F. Oliveira, Jr., and C. J. Quadros, J. Phys. E 2, 967 (1969).
[41]The term "coil foil" refers here to a tissue made of fine copper wires embedded in a thin sheet of G.E. 7031 varnish.

[42]D. M. Ginsberg and M. J. Melchner, Rev. Sci. Instrum. 41, 122 (1970).
[43]The basic design of capacitance dilatometers is discussed by G. K. White, Cryogenics 1, 151 (1961). Our design is slightly different, and avoids the necessity of drilling a hole in the sample.
[44]Y. Shapira and N. F. Oliveira, Jr., Phys. Rev. B 18, 1425 (1978).
[45]For discussions of demagnetization corrections see A. H. Morrish, *The Physical Principles of Magnetism* (Wiley, New York, 1965); and E. Stryjewski and N. Giordano, Adv. Phys. 26, 487 (1977).
[46]A small hysteresis was also observed in the screw-ferro transitions at finite $H$, and in the screw-fan transitions. All other transitions that were studied in the present work showed no noticeable hysteresis.
[47]E. Riedel and F. Wegner, Z. Phys. 225, 195 (1969).
[48]G. V. Lecomte, M. Karnezos, and S. A. Friedberg, J. Appl. Phys. 52, 1935 (1981).
[49]R. B. Griffiths, Phys. Rev. 7, 545 (1973); R. B. Griffiths and J. C. Wheeler, Phys. Rev. A 2, 1047 (1970).
[50]H. E. Stanley, T. S. Chang, F. Harbus, and L. L. Liu, in *Local Properties of Phase Transitions, Proceedings of the International School of Physics "Enrico Fermi," Course LIX* (North-Holland, Amsterdam, 1976); A. Hankey, H. E. Stanley, and T. S. Chang, Phys. Rev. Lett. 29, 278 (1972).
[51]T. S. Chang (unpublished).
[52]A. Michelson, Phys. Rev. B 16, 577 (1977).
[53]T. S. Chang, A. Hankey, and H. E. Stanley, Phys. Rev. B 8, 346 (1973).
[54]For scaling axes near a bicritical point, see M. E. Fisher, Phys. Rev. Lett. 34, 1634 (1975).
[55]D. Mukamel and M. Luban, Phys. Rev. B 18, 3631 (1978).
[56]M. D. Coutinho-Filho and M. A. de Moura, J. Magn. Magn. Mater. 15–18, 433 (1980).
[57]C. S. O. Yokoi, M. D. Coutinho-Filho, and S. R. Salinas (unpublished).
[58]J. M. Kosterlitz, D. R. Nelson, and M. E. Fisher, Phys. Rev. B 13, 412 (1976).
[59]D. P. Landau and K. Binder, Phys. Rev. B 17, 2328 (1978).
[60]W. J. Carr, Jr., in *Handbuch der Physik,* edited by S. Flügge (Springer-Verlag, Berlin, 1966), Vol. XVIII/2.
[61]In many theoretical discussions of the susceptibility in the ferro phase, the process of domain alignment is ignored. In such treatments, only the $H$-induced increase of the magnetization in a *single domain* is considered. However, to understand the experimentally observed susceptibility $\chi_m$, it is essential to include domain alignment in the analysis.
[62]Here we used Fig. 17 to relate the theoretical results in the $TP$ plane to the $H_b T$ plane of MnP.
[63]W. Selke, J. Magn. Magn. Mater. 9, 7 (1978).
[64]W. Selke, Phys. Lett. A 61, 443 (1977).